

HAT-P-20b–HAT-P-23b: FOUR MASSIVE TRANSITING EXTRASOLAR PLANETS[†]G. Á. BAKOS^{1,2}, J. HARTMAN¹, G. TORRES¹, D. W. LATHAM¹, GÉZA KOVÁCS³, R. W. NOYES¹, D. A. FISCHER^{4,5},
J. A. JOHNSON⁶, G. W. MARCY⁷, A. W. HOWARD⁷, D. KIPPING^{1,8}, G. A. ESQUERDO¹, A. SHPORER⁹, B. BÉKY¹,
L. A. BUCHHAVE¹⁰, G. PERUMPILLY¹, M. EVERETT¹, D. D. SASSELOV¹, R. P. STEFANIK¹, J. LÁZÁR¹¹, I. PAPP¹¹, P. SÁRI¹¹*Draft version October 22, 2018*

ABSTRACT

We report the discovery of four relatively massive (2–7 M_J) transiting extrasolar planets. **HAT-P-20b** orbits the moderately bright V=11.339 K3 dwarf star GSC 1910-00239 on a circular orbit, with a period $P = 2.875317 \pm 0.000004$ d, transit epoch $T_c = 2455080.92661 \pm 0.00021$ (BJD_{UTC}), and transit duration 0.0770 ± 0.0008 d. The host star has a mass of $0.76 \pm 0.03 M_\odot$, radius of $0.69 \pm 0.02 R_\odot$, effective temperature 4595 ± 80 K, and metallicity $[\text{Fe}/\text{H}] = +0.35 \pm 0.08$. The planetary companion has a mass of $7.246 \pm 0.187 M_J$, and radius of $0.867 \pm 0.033 R_J$ yielding a mean density of $13.78 \pm 1.50 \text{ g cm}^{-3}$, which is the second highest value among all known exoplanets. **HAT-P-21b** orbits the V=11.685 G3 dwarf star GSC 3013-01229 on an eccentric ($e = 0.228 \pm 0.016$) orbit, with a period $P = 4.124481 \pm 0.000007$ d, transit epoch $T_c = 2454996.41312 \pm 0.00069$, and transit duration 0.1530 ± 0.0027 d. The host star has a mass of $0.95 \pm 0.04 M_\odot$, radius of $1.10 \pm 0.08 R_\odot$, effective temperature 5588 ± 80 K, and metallicity $[\text{Fe}/\text{H}] = +0.01 \pm 0.08$. The planetary companion has a mass of $4.063 \pm 0.161 M_J$, and radius of $1.024 \pm 0.092 R_J$ yielding a mean density of $4.68^{+1.59}_{-0.99} \text{ g cm}^{-3}$. HAT-P-21b is a border-line object between the pM and pL class planets, and the transits occur near apastron. **HAT-P-22b** orbits the bright V=9.732 G5 dwarf star HD 233731 on a circular orbit, with a period $P = 3.212220 \pm 0.000009$ d, transit epoch $T_c = 2454930.22001 \pm 0.00025$, and transit duration 0.1196 ± 0.0014 d. The host star has a mass of $0.92 \pm 0.03 M_\odot$, radius of $1.04 \pm 0.04 R_\odot$, effective temperature 5302 ± 80 K, and metallicity $[\text{Fe}/\text{H}] = +0.24 \pm 0.08$. The planet has a mass of $2.147 \pm 0.061 M_J$, and compact radius of $1.080 \pm 0.058 R_J$ yielding a mean density of $2.11^{+0.40}_{-0.29} \text{ g cm}^{-3}$. The host star also harbors an M-dwarf companion at a wide separation. Finally, **HAT-P-23b** orbits the V=12.432 G0 dwarf star GSC 1632-01396 on a close to circular orbit, with a period $P = 1.212884 \pm 0.000002$ d, transit epoch $T_c = 2454852.26464 \pm 0.00018$, and transit duration 0.0908 ± 0.0007 d. The host star has a mass of $1.13 \pm 0.04 M_\odot$, radius of $1.20 \pm 0.07 R_\odot$, effective temperature 5905 ± 80 K, and metallicity $[\text{Fe}/\text{H}] = +0.15 \pm 0.04$. The planetary companion has a mass of $2.090 \pm 0.111 M_J$, and radius of $1.368 \pm 0.090 R_J$ yielding a mean density of $1.01 \pm 0.18 \text{ g cm}^{-3}$. HAT-P-23b is an inflated and massive hot Jupiter on a very short period orbit, and has one of the shortest characteristic in-fall times ($7.5^{+2.9}_{-1.8}$ Myr) before it gets engulfed by the star.

Subject headings: planetary systems — stars: individual (HAT-P-20, GSC 1910-00239, HAT-P-21, GSC 3013-01229, HAT-P-22, HD 233731, HAT-P-23, GSC 1632-01396) techniques: spectroscopic, photometric

1. INTRODUCTION

The majority of the ~ 90 known transiting extrasolar planets (TEPs) have been found to lie in the $0.5 M_J$ to $2.0 M_J$ mass range. The apparent drop in their mass distribution at $\sim 2 M_J$ has been noted by, e.g., Southworth et al. (2009), and by Torres et al. (2010). In the currently known sample, 75% of the TEPs have planetary mass $M_p < 2.0 M_J$, and there appears to be a minor peak in their occurrence rate at $M_p \approx 2 M_J$, which then sharply falls off towards higher masses. Are there any biases present against discovering massive planets? Such planets tend to be less inflated, and theory dictates that their radii shrink as their mass increases towards the brown dwarf regime. According to Baraffe, Chabrier, & Barman (2010), this reversal of the $M_p - R_p$ relation happens around $M_p \approx 2 - 3 M_J$, and falls off as $R_p \propto M_p^{-1/8}$ (see e.g. Fortney et al. 2009). The smaller radii for massive planets yield a minor bias against discovering them via the transit method, since they produce shallower transits. Very massive planets can induce stellar variability of their host stars (Shkolnik et al. 2009), somewhat decreasing the ef-

¹ Harvard-Smithsonian Center for Astrophysics, Cambridge, MA; email: gbakos@cfa.harvard.edu

² NSF Fellow

³ Konkoly Observatory, Budapest, Hungary

⁴ Astronomy Department, Yale University, New Haven, CT

⁵ Department of Physics and Astronomy, San Francisco State University, San Francisco, CA

⁶ California Institute of Technology, Department of Astrophysics, MC 249-17, Pasadena, CA

⁷ Department of Astronomy, University of California, Berkeley, CA

⁸ University College London, Dept. of Physics, Gower St., London, WC1E 6BT

⁹ LCOGT, 6740 Cortona Drive, Santa Barbara, CA, & Department of Physics, Broida Hall, UC Santa Barbara, CA

¹⁰ Niels Bohr Institute, Copenhagen University, DK-2100 Copenhagen, Denmark

¹¹ Hungarian Astronomical Association, Budapest, Hungary

[†] Based in part on observations obtained at the W. M. Keck Observatory, which is operated by the University of California and the California Institute of Technology. Keck time has been granted by NOAO and NASA.

efficiency of detecting their shallow transits via simple algorithms that expect constant out-of-transit light curves. Also, the host stars of massive planets are typically more rapid rotators: the average $v \sin i$ for host stars with planets $M_p < 2M_J$ is 3.9 ms^{-1} (with 3.8 ms^{-1} standard deviation around the mean), whereas the same values for the massive planet hosts stars, are 10.9 ms^{-1} (with 12.7 ms^{-1} standard deviation around the mean)¹³. The five fastest rotators all harbor planets more massive than $2M_J$. This presents a bias against discovering them either via radial velocity (RV) searches, which are more efficient around quiet non-rotating dwarfs, or via transit searches, where the targets may be discarded during the confirmation phase. Along the same lines, the large RV amplitude of the host star, as caused by the planetary companion, may even lead to erroneous rejection during the reconnaissance phase of candidate confirmation, since such systems resemble eclipsing binaries. Finally, there is a tendency that massive planets are more likely to be eccentric¹⁴ (Southworth et al. 2009), meaning that they require more RV observations for proper mapping of their orbits, and thus leading to a slower announcement rate. On the other hand, a strong bias *for* detecting such planets—compensating for most of the effects above—is the fact that the large RV amplitudes of the host stars are easier to detect, since they do not require internal precisions at the ms^{-1} level (see HAT-P-2, where valuable data was contributed to the RV fit by modest precision instruments yielding $\sim 1 \text{ km s}^{-1}$ precision; Bakos et al. 2007). Altogether, while there are minor biases for and against detecting massive transiting planets, their overall effect appears to be negligible, and the drop in frequency at $\gtrsim 2M_J$ seems to be real.

Massive planets are important for many reasons. They provide very strong constraints on formation and migration theories, which need to explain the observed distribution of planetary system parameters in a wide range (Baraffe et al. 2008; Baraffe, Chabrier, & Barman 2010), from $0.01 M_J$ (Corot-7b; Queloz et al. 2009) to $26.4 M_J$ (Corot-3b; Deleuil et al. 2008). Heavy mass objects necessitate the inclusion of other physical mechanisms for the formation and migration, such as planet-planet scattering (Chatterjee et al. 2008; Ford & Rasio 2008), and the Kozai-mechanism (Fabrycky & Tremaine 2007). They are border-line objects between planets and brown-dwarfs, and help us understand how these populations differ and overlap (see Leconte et al. 2009, for a review). For example, a traditional definition of planets is that they have no Deuterium burning, where the Deuterium burning limit is thought to be around $13 M_J$. However, there are large uncertainties on this limit due to the numerous model parameters and solutions, and the fact that Deuterium may be able to burn in the H/He layers above the core (Baraffe et al. 2008). Another possible definition of planets is based on their formation scenario, i.e. they are formed by accretion in a protoplanetary disk around their young host star, as opposed to the gravitational collapse of a molecular cloud (brown dwarfs).

Perhaps related to the formation and migration mechanisms, a number of interesting correlations involving massive planets have been pointed out.

Udry et al. (2002) noted that short period massive planets are predominantly found in binary stellar systems. Southworth et al. (2009) noted that only 8.6% of the low mass planets show significantly eccentric orbits, whereas 77% of the massive planets have eccentric orbits (although low-mass systems have lower S/N RV curves, rendering the detection of eccentric orbits more difficult). Curiously, there appears to be a lack of correlation between planetary mass and host star metallicity, while one would naively think that the formation of high mass planets (via core accretion) would require higher metal content. Until this work, there was a hint of a correlation between planetary and stellar mass (e.g. Deleuil et al. 2008), in the sense that the most massive planets orbited $M_\star \gtrsim 1.2 M_\odot$ stars, and there was a (biased) tendency that lower mass planets orbit less massive stars.

All of these observations suffer from small-number statistics and heavy biases. One way of improving our knowledge is to expand the sample of well-characterized planets. In this work we report on 4 new massive transiting planets around bright stars, namely GSC 1910-00239, GSC 3013-01229, HD 233731, and GSC 1632-01396. This extends the currently known sample of bright ($V < 13.5$) and massive ($M_p > 2M_J$) transiting planets by 30% (from 13 to 17). These discoveries were made by the Hungarian-made Automated Telescope Network (HATNet; Bakos et al. 2004) survey. HATNet has been one of the main contributors to the discovery of TEPs, among others such as the ground-based Super-WASP (Pollacco et al. 2006), TrES (Alonso et al. 2004) and XO projects (McCullough et al. 2005), and space-borne searches such as CoRoT (Baglin et al. 2006) and Kepler (Borucki et al. 2010). In operation since 2003, HATNet has now covered approximately 14% of the sky, searching for TEPs around bright stars ($8 \lesssim I \lesssim 14$). We operate six wide-field instruments: four at the Fred Lawrence Whipple Observatory (FLWO) in Arizona, and two on the roof of the hangar servicing the Smithsonian Astrophysical Observatory’s Submillimeter Array, in Hawaii.

The layout of the paper is as follows. In Section 2 we report the detections of the photometric signals and the follow-up spectroscopic and photometric observations for each of the planets. In Section 3 we describe the analysis of the data, beginning with the determination of the stellar parameters, continuing with a discussion of the methods used to rule out nonplanetary, false positive scenarios which could mimic the photometric and spectroscopic observations, and finishing with a description of our global modeling of the photometry and radial velocities. Our findings are discussed in Section 4.

2. OBSERVATIONS

2.1. Photometric detection

Table 1 summarizes the HATNet discovery observations of each new planetary system. The calibration of the HATNet frames was carried out using standard procedures correcting for the CCD bias, dark-current and flatfield structure. The calibrated images were then subjected to star detection and astrometry, as described in Pál & Bakos (2006). Aperture photometry was performed on each image at the stellar centroids derived from the Two Micron All Sky Survey (2MASS;

¹³ This includes those 4 planets announced in this paper.

¹⁴ See e.g. exoplanets.org for statistics.

Skrutskie et al. 2006) catalog and the individual astrometric solutions. For certain datasets (HAT-P-20, HAT-P-22, HAT-P-23) we also carried out an image subtraction (Alard 2000) based photometric reduction using discrete kernels (Bramich 2008), as described in Pál (2009b). The resulting light curves were decorrelated (cleaned of trends) using the External Parameter Decorrelation (EPD; see Bakos et al. 2010) technique in “constant” mode and the Trend Filtering Algorithm (TFA; see Kovács et al. 2005). The light curves were searched for periodic box-shaped signals using the Box Least-Squares (BLS; see Kovács et al. 2002) method. We detected significant signals in the light curves of the stars as summarized below:

- *HAT-P-20* – GSC 1910-00239 (also known as 2MASS 07273995+2420118; $\alpha = 07^{\text{h}}27^{\text{m}}39.96^{\text{s}}$, $\delta = +24^{\circ}20'11.9''$; J2000; $V=11.339$). A signal was detected for this star with an apparent depth of ~ 10.8 mmag, and a period of $P = 2.8753$ days (see Figure 1). Note that the depth was attenuated by the presence of the fainter neighbor star that is not resolved on the coarse resolution ($14''\text{pixel}^{-1}$) HATNet pixels. Also, the depth by fitting a trapeze instead of the correct Mandel & Agol (2002) model, is somewhat shallower than the maximum depth in the Mandel & Agol (2002) model fit (which was 19.6 mmag; see later in § 3.3). The drop in brightness had a first-to-last-contact duration, relative to the total period, of $q = 0.0268 \pm 0.0003$, corresponding to a total duration of $Pq = 1.848 \pm 0.019$ hr. HAT-P-20 has a red companion (2MASS 07273963+2420171, $J - K = 0.92$) at $6.86''$ separation that is fainter than HAT-P-20 by $\Delta R = 1.36$ mag.
- *HAT-P-21* – GSC 3013-01229 (also known as 2MASS 11250598+4101406; $\alpha = 11^{\text{h}}25^{\text{m}}05.88^{\text{s}}$, $\delta = +41^{\circ}01'40.6''$; J2000; $V=11.685$). A signal was detected for this star with an apparent depth of ~ 8.0 mmag, and a period of $P = 4.1245$ days (see Figure 2). The drop in brightness had a first-to-last-contact duration, relative to the total period, of $q = 0.0371 \pm 0.0007$, corresponding to a total duration of $Pq = 3.672 \pm 0.065$ hr.
- *HAT-P-22* – HD 233731 (also known as GSC 03441-00925 and 2MASS 10224361+5007420; $\alpha = 10^{\text{h}}22^{\text{m}}43.68^{\text{s}}$, $\delta = +50^{\circ}07'42.0''$; J2000; $V=9.732$). A signal was detected for this star with an apparent depth of ~ 9.7 mmag, and a period of $P = 3.2122$ days (see Figure 3). The drop in brightness had a first-to-last-contact duration, relative to the total period, of $q = 0.0372 \pm 0.0004$, corresponding to a total duration of $Pq = 2.869 \pm 0.033$ hr. HAT-P-22 has a close red companion star (2MASS 10224397+5007504, $J - K = 0.86$) at $9.1''$ separation and $\Delta i = 2.58$ magnitude fainter.
- *HAT-P-23* – GSC 1632-01396 (also known as 2MASS 20242972+1645437; $\alpha = 20^{\text{h}}24^{\text{m}}29.88^{\text{s}}$, $\delta = +16^{\circ}45'43.7''$; J2000; $V=12.432$). A signal was detected for this star with an apparent depth of ~ 11.5 mmag, and a period of $P = 1.2129$ days (see

Figure 4). Similarly to HAT-P-20, the depth was attenuated by close-by faint neighbors. The drop in brightness had a first-to-last-contact duration, relative to the total period, of $q = 0.0748 \pm 0.0006$, corresponding to a total duration of $Pq = 2.178 \pm 0.017$ hr.

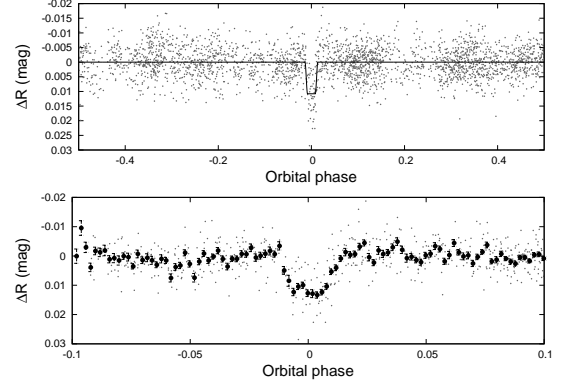


FIG. 1.— Unbinned light curve of HAT-P-20 including all 2600 instrumental R band 5.5 minute cadence measurements obtained with the HAT-7 and HAT-8 telescopes of HATNet (see Table 1 for details), and folded with the period $P = 2.8753172$ days resulting from the global fit described in Section 3. The solid line shows the “P1P3” transit model fit to the light curve (Section 3.3). The bold points in the lower panel show the light curve binned in phase with a bin-size of 0.002.

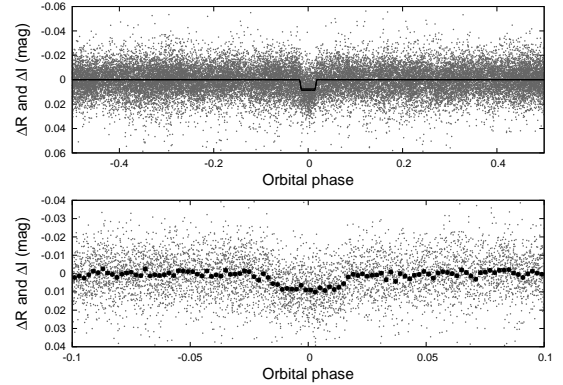


FIG. 2.— Unbinned light curve of HAT-P-21 including all 28,000 instrumental I band and R band 5.5 minute cadence measurements obtained with the HAT-5, HAT-6, HAT-8 and HAT-9 telescopes of HATNet (see Table 1 for details), and folded with the period $P = 4.1244808$ days resulting from the global fit described in Section 3. The solid line shows the “P1P3” transit model fit to the light curve (Section 3.3). The bold points in the lower panel show the light curve binned in phase with a bin-size of 0.002.

2.2. Reconnaissance Spectroscopy

As is routine in the HATNet project, all candidates are subjected to careful scrutiny before investing valuable time on large telescopes. This includes spectroscopic observations at relatively modest facilities to establish whether the transit-like feature in the light curve of a candidate might be due to astrophysical phenomena other than a planet transiting a star. Many of these false positives are associated with large radial-velocity variations in the star (tens of km s^{-1}) that are easily recognized. The reconnaissance spectroscopic observations

TABLE 1
SUMMARY OF PHOTOMETRIC OBSERVATIONS

Instrument/Field	Date(s)	Number of Images	Cadence (s)	Filter
HAT-P-20				
HAT-7/G267	2007 Dec–2008 May	802	330	<i>R</i>
HAT-8/G267	2007 Oct–2008 May	1850	330	<i>R</i>
KeplerCam	2009 Mar 11	268	43	Sloan <i>i</i>
KeplerCam	2009 Oct 21	343	32	Sloan <i>i</i>
HAT-P-21				
HAT-6/G183	2006 Dec–2007 May	4528	330	<i>I</i>
HAT-9/G183	2006 Nov–2007 Jun	4586	330	<i>I</i>
HAT-5/G184	2006 Dec–2007 Jun	4040	330	<i>I</i>
HAT-8/G184	2006 Dec–2007 Jun	5606	330	<i>I</i>
HAT-6/G141	2008 Jan–2008 Jun	5142	330	<i>R</i>
HAT-9/G141	2008 Jan–2008 Jun	3964	330	<i>R</i>
KeplerCam	2009 Apr 20	243	53	Sloan <i>i</i>
KeplerCam	2010 Feb 15	412	43	Sloan <i>i</i>
FTN/LCOGT ^a	2010 Feb 19	511	31	Sloan <i>i</i>
HAT-P-22				
HAT-5/G139	2007 Dec–2008 May	4288	330	<i>R</i>
KeplerCam	2009 Feb 28	532	28	Sloan <i>z</i>
KeplerCam	2009 Apr 30	353	33	Sloan <i>g</i>
HAT-P-23				
HAT-6/G341	2007 Sep–2007 Dec	1178	330	<i>R</i>
HAT-9/G341	2007 Sep–2007 Nov	2351	330	<i>R</i>
KeplerCam	2008 Jun 14	147	73	Sloan <i>i</i>
KeplerCam	2008 Sep 08	246	73	Sloan <i>i</i>
KeplerCam	2008 Sep 13	265	73	Sloan <i>i</i>
KeplerCam	2008 Nov 03	117	89	Sloan <i>i</i>
KeplerCam	2009 Apr 19	46	150	Sloan <i>g</i>
KeplerCam	2009 Jul 13	150	73	Sloan <i>i</i>

^a Observations were performed without guiding due to a technical problem with the guiding system, and resulted in decreased data quality.

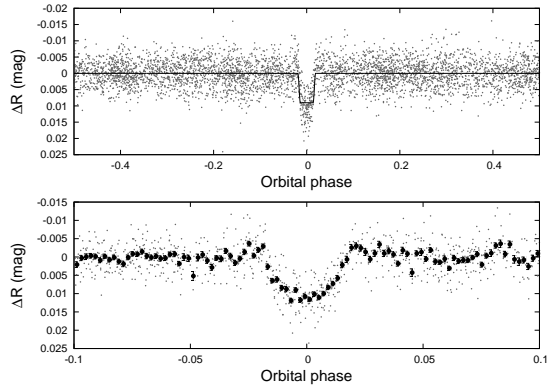


FIG. 3.— Unbinned light curve of HAT-P-22 including all 4200 instrumental *R* band 5.5 minute cadence measurements obtained with the HAT-5 telescope of HATNet (see the text for details), and folded with the period $P = 3.2122198$ days resulting from the global fit described in Section 3. The solid line shows the “P1P3” transit model fit to the light curve (Section 3.3). The bold points in the lower panel show the light curve binned in phase with a bin-size of 0.002.

and results for each system are summarized in Table 2; below we provide a brief description of the instruments used, the data reduction, and the analysis procedure.

One of the tools we have used for this purpose is the Harvard-Smithsonian Center for Astrophysics (CfA) Digital Speedometer (DS; Latham 1992), an echelle spectrograph mounted on the FLWO 1.5 m telescope. This instrument delivers high-resolution spectra ($\lambda/\Delta\lambda \approx 35,000$) over a single order centered on the Mg Ib triplet ($\sim 5187 \text{ \AA}$), with typically low signal-to-noise (S/N) ra-

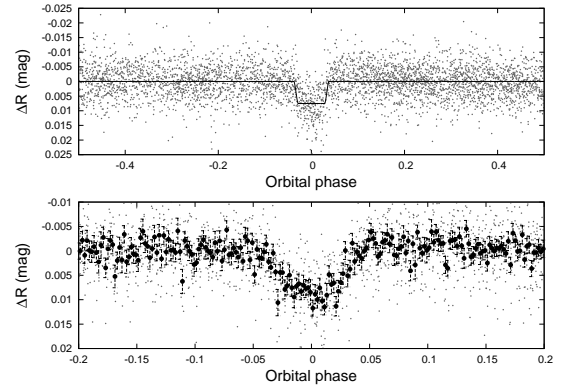


FIG. 4.— Unbinned light curve of HAT-P-23 including all 3500 instrumental *R* band 5.5 minute cadence measurements obtained with the HAT-6 and HAT-9 telescopes of HATNet (see Table 1 for details), and folded with the period $P = 1.2128841$ days resulting from the global fit described in Section 3. The solid line shows the “P1P3” transit model fit to the light curve (Section 3.3). The bold points in the lower panel show the light curve binned in phase with a bin-size of 0.002.

tios that are nevertheless sufficient to derive radial velocities (RVs) with moderate precisions of $0.5\text{--}1.0 \text{ km s}^{-1}$ for slowly rotating stars. The same spectra can be used to estimate the effective temperature, surface gravity, and projected rotational velocity of the host star, as described by Torres et al. (2002). With this facility we are able to reject many types of false positives, such as F dwarfs orbited by M dwarfs, grazing eclipsing binaries, or triple or quadruple star systems. Additional tests are performed with other spectroscopic material described in the next

section.

Another of the tools we have used for this purpose is the Fibre-fed Échelle Spectrograph (FIES) at the 2.5 m Nordic Optical Telescope (NOT) at La Palma, Spain (Djupvik & Andersen 2010). We used the medium-resolution fiber which produces spectra at a resolution of $\lambda/\Delta\lambda \approx 46,000$ and a wavelength coverage of $\sim 3600\text{--}7400\text{ \AA}$ to observe HAT-P-20. The spectrum was extracted and analyzed to measure the radial velocity, effective temperature, surface gravity, and projected rotation velocity of the host star, following the procedures described by Buchhave et al. (2010).

Based on the observations summarized in Table 2 we find that HAT-P-21, HAT-P-22 and HAT-P-23 have rms residuals consistent with no detectable RV variation within the precision of the measurements. Curiously, HAT-P-20 showed significant RV variations, even at the modest ($\sim 0.5\text{ km s}^{-1}$) precision of the Digital Speedometer, and the reconnaissance RV variations (including the FIES spectrum; see later) phased up with the photometric ephemeris. All spectra were single-lined, i.e., there is no evidence that any of these targets consist of more than one star. The gravities for all of the stars indicate that they are dwarfs.

2.3. High resolution, high S/N spectroscopy

We proceeded with the follow-up of each candidate by obtaining high-resolution, high-S/N spectra to characterize the RV variations, and to refine the determination of the stellar parameters. These observations are summarized in Table 3. The RV measurements and uncertainties are given in Table 4, Table 5, Table 6 and Table 7 for HAT-P-20 through HAT-P-23, respectively. The period-folded data, along with our best fits described below in Section 3, are displayed in Figure 6 through Figure 9 for HAT-P-20 through HAT-P-23. Below we briefly describe the instruments used, the data reduction, and the analysis procedure.

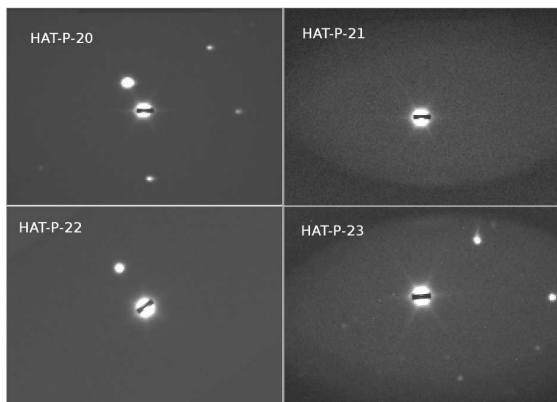


FIG. 5.— Keck/HIRES guider camera snapshots of HAT-P-20 through HAT-P-23 (labeled). North is up and East is to the left. The snapshots cover an area of approximately $30 \times 20''$. The slit is also visible, as positioned on the planet host stars.

Observations were made of all four planet host stars with the HIRES instrument (Vogt et al. 1994) on the Keck I telescope located on Mauna Kea, Hawaii. The width of the spectrometer slit was $0''.86$, resulting in a resolving power of $\lambda/\Delta\lambda \approx 55,000$, with a wavelength cov-

erage of $\sim 3800\text{--}8000\text{ \AA}$. We typically used the B5 decker yielding a $3.5''(H) \times 0.861''(W)$ slit, and for the last few observations on each target we used the C2 decker that enables a better sky subtraction due to the longer slit $14.0''(H) \times 0.861''(W)$. The slit height was oriented with altitude (vertical), except for rare cases, when the slit would have run through the faint companion to HAT-P-20 or HAT-P-22. A Keck/HIRES snapshot for each planet host star is shown in Figure 5. Spectra were obtained through an iodine gas absorption cell, which was used to superimpose a dense forest of I_2 lines on the stellar spectrum and establish an accurate wavelength fiducial (see Marcy & Butler 1992). For each target an additional exposure was taken without the iodine cell, for use as a template in the reductions. Relative RVs in the solar system barycentric frame were derived as described by Butler et al. (1996), incorporating full modeling of the spatial and temporal variations of the instrumental profile.

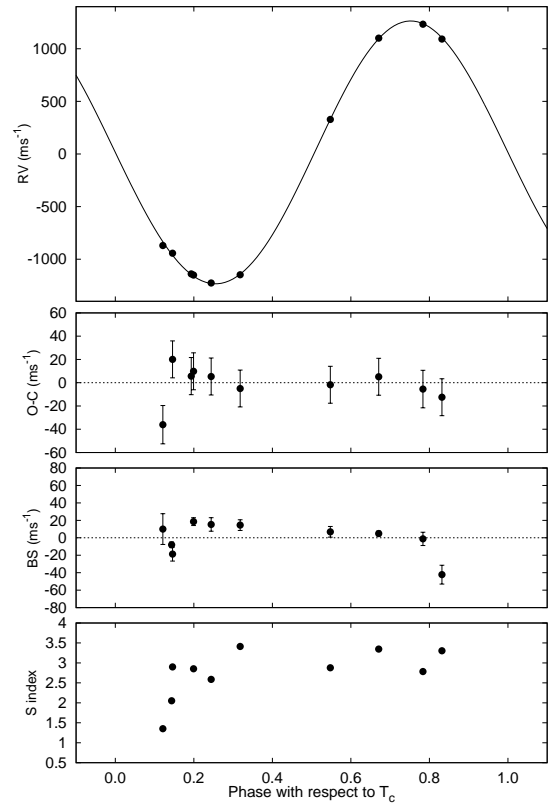


FIG. 6.— *Top panel:* Keck/HIRES RV measurements for HAT-P-20 shown as a function of orbital phase, along with our best-fit eccentric model (see Table 14). Zero phase corresponds to the time of mid-transit. The center-of-mass velocity has been subtracted. The rms around the best orbital fit is 16.2 ms^{-1} . *Second panel:* Velocity $O-C$ residuals from the best fit. The error bars for both the top and second panel include a component from the jitter (15.7 ms^{-1}) added in quadrature to the formal errors (see Section 3.3). *Third panel:* Bisector spans (BS), with the mean value subtracted. The measurement from the template spectrum is included (see Section 3.2). *Bottom panel:* Relative chromospheric activity index S measured from the Keck spectra.

In each of Figures 6–9 we show also the relative S index, which is a measure of the chromospheric activity of the star derived from the flux in the cores of the Ca II H and K lines. This index was computed following the pre-

TABLE 2
SUMMARY OF RECONNAISSANCE SPECTROSCOPY OBSERVATIONS

Instrument	Date(s)	Number of Spectra	$T_{\text{eff}\star}$ (K)	$\log g_{\star}$ (cgs)	$v \sin i$ (km s ⁻¹)	$\gamma_{\text{RV}}^{\text{a}}$ (km s ⁻¹)
HAT-P-20						
DS	2009 Feb 11–2009 Feb 15	3	4500 ± 125	4.0 ± 0.25	0 ± 4	-18.81 ± 0.68
FIES	2009 Oct 07	1	4500	4.0	4	-16.76 ± 0.1
HAT-P-21						
DS	2009 Mar 08–2009 Apr 05	3	5750 ± 125	4.5 ± 0.25	3.0 ± 3.0	-53.19 ± 0.09
HAT-P-22						
DS	2009 Feb 11–2009 Feb 16	4	5250 ± 125	4.5 ± 0.25	2.0 ± 2.0	$+12.49 \pm 0.28$
HAT-P-23						
DS	2008 May 19–2008 Sep 14	5	6000 ± 125	4.5 ± 0.25	9.0 ± 1.0	-15.10 ± 0.30

^a The mean heliocentric RV of the target (in the IAU system). The error gives the rms of the individual velocity measures for the target with the given instrument.

TABLE 3
SUMMARY OF HIGH-RESOLUTION/HIGH-SN
SPECTROSCOPIC OBSERVATIONS

Instrument	Date(s)	Number of RV obs.
HAT-P-20		
Keck/HIRES	2009 Apr–2009 Dec	10
HAT-P-21		
Keck/HIRES	2009 May–2010 Feb	15
HAT-P-22		
Keck/HIRES	2009 Apr–2009 Dec	12
HAT-P-23		
Keck/HIRES	2008 Jun–2009 Dec	13

scription given by Vaughan, Preston & Wilson (1978), and as described in Hartman et al. (2009). Note that our relative S index has not been calibrated to the scale of Vaughan, Preston & Wilson (1978). We do not detect any significant variation of the index correlated with orbital phase; such a correlation might have indicated that the RV variations could be due to stellar activity, casting doubt on the planetary nature of the candidate. There is no sign of emission in the cores of the Ca II H and K lines in any of our spectra, from which we conclude that all of the targets have low chromospheric activity levels.

2.4. Photometric follow-up observations

In order to permit a more accurate modeling of the light curves, we conducted additional photometric observations with the KeplerCam CCD camera on the FLWO 1.2m telescope for each star, and with the Faulkes North Telescope (FTN) of the Las Cumbres Observatory Global Network (LCOGT) at Hawaii for HAT-P-21 only. The observations for each target are summarized in Table 1.

The reduction of these images, including basic calibration, astrometry, and aperture photometry, was performed as described by Bakos et al. (2010). We found that the aperture photometry for HAT-P-20 was significantly affected by the close-by neighbor star 2MASS 07273995+2420118 with $\Delta i = 1.1$ magnitude difference at $6.86''$ separation (Figure 5). Thus, we performed image subtraction on the FLWO 1.2m images with the

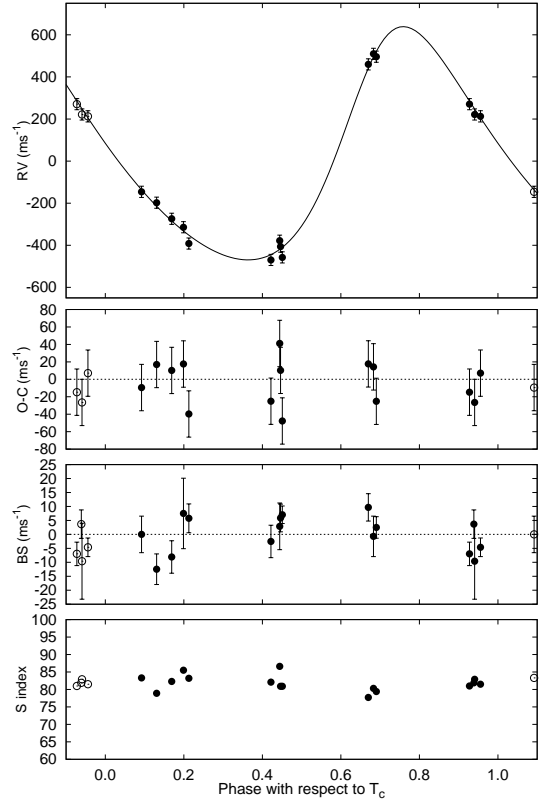


FIG. 7.— Keck/HIRES observations of HAT-P-21. The panels are as in Figure 6. The parameters used in the best-fit model are given in Table 14, the RV jitter was 26.4 m s^{-1} , and the fit rms was 26.6 m s^{-1} . Observations shown twice are represented with open symbols.

same toolset used for the HATNet reductions, but applied a discrete kernel with half-size of 5 pixels and no spatial variations. Indeed, for this stellar configuration, the image subtraction results proved to be superior to the aperture photometry. For all of the follow-up light curves, we performed EPD and TFA to remove trends simultaneously with the light curve modeling (for more details, see Section 3, and Bakos et al. 2010). The final time series, together with our best-fit transit light curve model, are shown in the top portion of Figures 10 through 13; the individual measurements are reported in

TABLE 4
RELATIVE RADIAL VELOCITIES, BISECTOR SPANS, AND ACTIVITY INDEX
MEASUREMENTS OF HAT-P-20.

BJD _{UTC} ^a (2,454,000+)	RV ^b (m s ⁻¹)	σ_{RV} ^c (m s ⁻¹)	BS (m s ⁻¹)	σ_{BS} (m s ⁻¹)	S ^d	σ_S
934.84149 .	-1139.51	2.94
954.82485	-8.00	3.22	2.051	0.075
954.83175 ..	-942.88	2.24	-18.65	8.02	2.900	0.035
956.80481 ..	1092.32	2.28	-42.21	10.81	3.305	0.018
983.73851 ..	-1151.02	2.39	18.53	4.51	2.853	0.016
984.74064 ..	328.09	2.14	6.85	6.11	2.879	0.016
986.74296 ..	-1225.77	2.34	15.28	7.78	2.588	0.029
1107.15226 .	-870.02	4.89	10.00	17.65	1.352	0.043
1109.05752 .	1233.55	3.76	-1.23	7.66	2.783	0.018
1191.10274 .	-1147.72	2.07	14.55	6.16	3.412	0.016
1192.11754 .	1100.72	2.12	4.88	2.83	3.346	0.015

NOTE. — Note that for the iodine-free template exposures we do not measure the RV but do measure the BS and S index. Such template exposures can be distinguished by the missing RV value.

^a Barycentric Julian dates throughout the paper are calculated from Coordinated Universal Time (UTC).

^b The zero-point of these velocities is arbitrary. An overall offset γ_{rel} fitted to these velocities in Section 3.3 has *not* been subtracted.

^c Internal errors excluding the component of astrophysical jitter considered in Section 3.3.

^d Relative chromospheric activity index, not calibrated to the scale of Vaughan, Preston & Wilson (1978).

TABLE 5
RELATIVE RADIAL VELOCITIES, BISECTOR SPANS, AND ACTIVITY INDEX
MEASUREMENTS OF HAT-P-21.

BJD _{UTC} ^a (2,454,000+)	RV ^a (m s ⁻¹)	σ_{RV} ^b (m s ⁻¹)	BS (m s ⁻¹)	σ_{BS} (m s ⁻¹)	S ^c	σ_S
954.91548	3.67	5.10	0.819	0.002
954.92307 ..	221.51	2.88	-9.60	13.62	0.829	0.003
955.86532 ..	-274.01	2.48	-8.08	5.81	0.823	0.003
955.98849 ..	-314.29	2.76	7.51	12.62	0.855	0.005
957.00006 ..	-378.18	3.00	2.88	8.36	0.866	0.009
963.95573 ..	-197.70	2.68	-12.46	5.48	0.789	0.003
983.85638 ..	212.70	2.72	-4.61	3.33	0.815	0.003
985.87988 ..	-406.23	2.46	5.88	4.95	0.809	0.003
986.85645 ..	509.76	3.01	-0.70	7.24	0.803	0.005
987.86480 ..	270.66	2.92	-6.96	4.20	0.810	0.004
1174.14589 .	-145.85	3.13	0.01	6.54	0.833	0.005
1191.14119 .	-391.67	2.75	5.76	5.16	0.832	0.005
1192.12302 .	-457.57	2.67	7.04	3.15	0.809	0.005
1193.11001 .	496.07	2.58	2.50	3.85	0.794	0.005
1197.15057 .	459.61	2.59	9.69	4.91	0.777	0.005
1229.12322 .	-469.62	2.81	-2.53	5.81	0.821	0.005

NOTE. — Notes for this table are identical to that of Table 4.

Tables 8—11, for HAT-P-20 through HAT-P-23, respectively.

3. ANALYSIS

3.1. Properties of the parent stars

Fundamental parameters for each of the host stars, including the mass (M_*) and radius (R_*), which are needed to infer the planetary properties, depend strongly on other stellar quantities that can be derived spectroscopically. For this we have relied on our template spectra obtained with the Keck/HIRES instrument, and the analysis package known as Spectroscopy Made Easy (SME; Valenti & Piskunov 1996), along with the atomic line database of Valenti & Fischer (2005). For each star, SME yielded the following *initial* values and uncertainties (which we have conservatively increased to include

our estimates of the systematic errors):

- *HAT-P-20* – effective temperature $T_{\text{eff}\star} = 4626 \pm 104$ K, stellar surface gravity $\log g_\star = 4.80 \pm 0.06$ (cgs), metallicity $[\text{Fe}/\text{H}] = +0.31 \pm 0.08$ dex, and projected rotational velocity $v \sin i = 3.1 \pm 0.5$ km s⁻¹.
- *HAT-P-21* – effective temperature $T_{\text{eff}\star} = 5701 \pm 144$ K, stellar surface gravity $\log g_\star = 4.48 \pm 0.14$ (cgs), metallicity $[\text{Fe}/\text{H}] = +0.04 \pm 0.1$ dex, and projected rotational velocity $v \sin i = 4.1 \pm 0.5$ km s⁻¹.
- *HAT-P-22* – effective temperature $T_{\text{eff}\star} = 5338 \pm 88$ K, stellar surface gravity $\log g_\star = 4.52 \pm 0.14$ (cgs), metallicity $[\text{Fe}/\text{H}] = +0.26 \pm 0.08$ dex,

TABLE 6
RELATIVE RADIAL VELOCITIES, BISECTOR SPANS, AND ACTIVITY INDEX
MEASUREMENTS OF HAT-P-22.

BJD _{UTC} (2,454,000+)	RV ^a (m s ⁻¹)	σ_{RV}^b (m s ⁻¹)	BS (m s ⁻¹)	σ_{BS} (m s ⁻¹)	S ^c	σ_S
928.94934 .	187.55	1.12	13.71	4.73	0.557	0.002
954.88137 ..	284.38	1.12	7.07	3.69	0.556	0.002
954.88605	-2.17	3.34	0.554	0.001
955.79962 ..	77.44	1.46	6.00	13.88	0.533	0.008
956.96383 ..	-273.80	1.30	4.41	10.92	0.531	0.005
963.92157 ..	-14.63	1.33	-0.17	6.57	0.570	0.002
983.82710 ..	282.58	0.98	2.20	3.79	0.572	0.003
985.81064 ..	-298.55	1.14	-2.81	2.96	0.560	0.002
986.84124 ..	239.74	1.39	-7.48	6.58	0.553	0.003
988.83025 ..	-300.15	1.31	-16.80	8.24	0.555	0.002
1191.14866 .	-326.24	1.32	-0.33	5.00	0.843	0.003
1193.10170 .	255.62	1.30	-8.71	6.79	0.835	0.003
1193.93435 .	-192.43	1.38	5.08	5.27	0.843	0.004

NOTE. — Notes for this table are identical to that of Table 4.

TABLE 7
RELATIVE RADIAL VELOCITIES, BISECTOR SPANS, AND ACTIVITY INDEX
MEASUREMENTS OF HAT-P-23.

BJD _{UTC} (2,454,000+)	RV ^a (m s ⁻¹)	σ_{RV}^b (m s ⁻¹)	BS (m s ⁻¹)	σ_{BS} (m s ⁻¹)	S ^c	σ_S
638.09243	-4.89	4.59	1.170	0.020
638.10601 ..	-137.90	4.49	-0.45	5.22	0.797	0.006
674.91404 ..	374.64	5.15	-10.71	3.99	0.794	0.006
723.78719 ..	-209.16	5.55	-1.68	13.38	0.738	0.006
725.85309 ..	329.57	6.18	12.86	6.55	0.749	0.006
726.87976 ..	277.98	4.20	-26.82	6.17	0.770	0.005
727.76247 ..	-210.01	4.81	-35.11	5.18	0.811	0.006
727.89619 ..	-19.91	4.77	-30.29	5.05	0.795	0.005
777.82189 ..	214.73	4.54	-12.64	4.43	0.754	0.005
810.72960 ..	290.22	5.63	-13.57	5.59	0.726	0.006
955.04676 ..	388.82	4.74	-15.76	3.57	0.761	0.006
985.99494 ..	-369.93	4.42	-19.69	5.06	0.718	0.006
1192.70812 .	348.01	4.40	-14.40	4.53	0.726	0.005
1193.71080 .	83.68	4.57	-20.67	4.23	0.825	0.008

NOTE. — Notes for this table are identical to that of Table 4.

TABLE 8
HIGH-PRECISION DIFFERENTIAL PHOTOMETRY OF HAT-P-20.

BJD _{UTC} (2,400,000+)	Mag ^a	σ_{Mag}	Mag(orig) ^b	Filter
54902.59749	-0.00169	0.00075	10.66286	<i>i</i>
54902.59799	-0.00139	0.00075	10.66200	<i>i</i>
54902.59848	-0.00469	0.00075	10.65893	<i>i</i>
54902.59919	0.00281	0.00075	10.66596	<i>i</i>
54902.59970	-0.00108	0.00075	10.66316	<i>i</i>
54902.60020	0.00141	0.00075	10.66524	<i>i</i>
54902.60089	0.00440	0.00075	10.66726	<i>i</i>
54902.60139	0.00040	0.00075	10.66424	<i>i</i>
54902.60190	-0.00064	0.00075	10.66234	<i>i</i>
54902.60259	-0.00009	0.00075	10.66388	<i>i</i>

NOTE. — This table is available in a machine-readable form in the online journal. A portion is shown here for guidance regarding its form and content.

^a The out-of-transit level has been subtracted. These magnitudes have been subjected to the EPD and TFA procedures, carried out simultaneously with the transit fit.

^b Raw magnitude values without application of the EPD and TFA procedures.

and projected rotational velocity $v \sin i = 1.5 \pm 0.5 \text{ km s}^{-1}$.

TABLE 9
HIGH-PRECISION DIFFERENTIAL PHOTOMETRY OF HAT-P-21.

BJD _{UTC} (2,400,000+)	Mag ^a	σ_{Mag}	Mag(orig) ^b	Filter
54942.76369	0.01133	0.00088	10.43700	<i>i</i>
54942.76432	0.01370	0.00088	10.43950	<i>i</i>
54942.76495	0.00989	0.00088	10.43550	<i>i</i>
54942.76574	0.00891	0.00088	10.43490	<i>i</i>
54942.76637	0.00974	0.00088	10.43570	<i>i</i>
54942.76698	0.01073	0.00088	10.43650	<i>i</i>
54942.76779	0.00961	0.00088	10.43480	<i>i</i>
54942.76839	0.00938	0.00088	10.43450	<i>i</i>
54942.76902	0.01249	0.00088	10.43800	<i>i</i>
54942.76980	0.01011	0.00088	10.43520	<i>i</i>

NOTE. — Notes for this table are identical to those of Table 8.

- *HAT-P-23* – effective temperature $T_{\text{eff}\star} = 5987 \pm 120 \text{ K}$, stellar surface gravity $\log g_{\star} = 4.48 \pm 0.12 \text{ (cgs)}$, metallicity $[\text{Fe}/\text{H}] = +0.18 \pm 0.1 \text{ dex}$, and projected rotational velocity $v \sin i = 8.0 \pm 0.5 \text{ km s}^{-1}$.

In principle the effective temperature and metallicity, along with the surface gravity taken as a luminosity in-

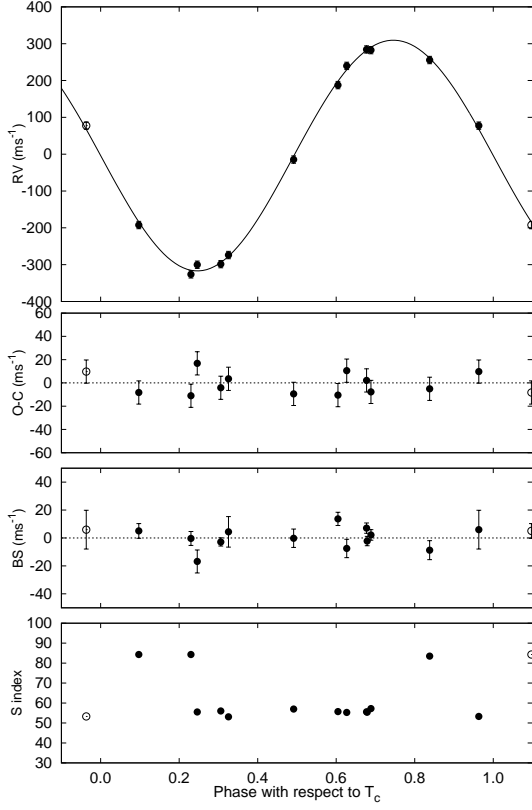


FIG. 8.— Keck/HIRES observations of HAT-P-22. The panels are as in Figure 6. The parameters used in the best-fit model are given in Table 14, the RV jitter was 9.9 m s^{-1} , and the fit rms was 10.0 m s^{-1} . Observations shown twice are represented with open symbols.

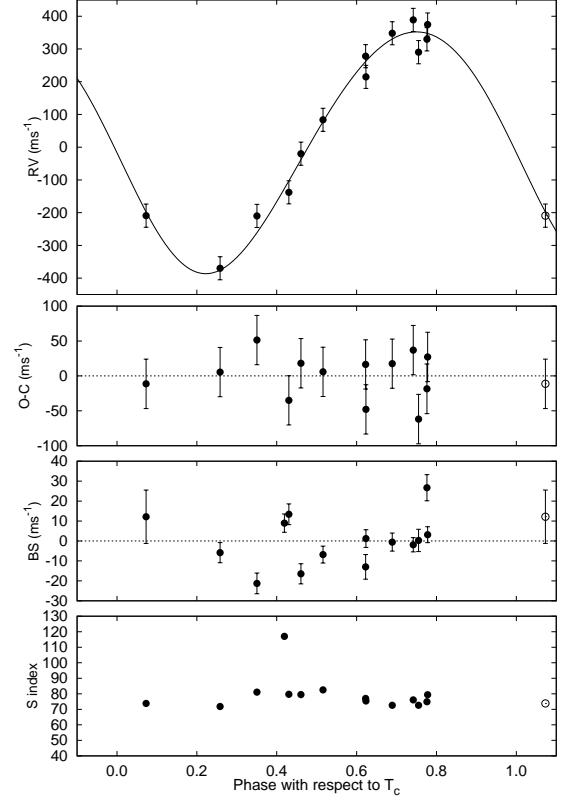


FIG. 9.— Keck/HIRES observations of HAT-P-23. The panels are as in Figure 6. The parameters used in the best-fit model are given in Table 14, and the RV jitter was 34.7 m s^{-1} . Observations shown twice are represented with open symbols.

TABLE 10
HIGH-PRECISION DIFFERENTIAL PHOTOMETRY OF HAT-P-22.

BJD _{UTC} (2,400,000+)	Mag ^a	σ_{Mag}	Mag(orig) ^b	Filter
54891.60570	0.00028	0.00069	8.78803	<i>z</i>
54891.60603	-0.00100	0.00069	8.78658	<i>z</i>
54891.60636	-0.00189	0.00069	8.78541	<i>z</i>
54891.60667	-0.00138	0.00069	8.78514	<i>z</i>
54891.60702	-0.00237	0.00069	8.78534	<i>z</i>
54891.60735	0.00030	0.00069	8.78923	<i>z</i>
54891.60767	0.00404	0.00069	8.79234	<i>z</i>
54891.60801	-0.00170	0.00069	8.78696	<i>z</i>
54891.60831	0.00257	0.00069	8.79009	<i>z</i>
54891.60865	-0.00145	0.00069	8.78653	<i>z</i>

NOTE. — Notes for this table are identical to those of Table 8.

indicator, could be used as constraints to infer the stellar mass and radius by comparison with stellar evolution models. However, the effect of $\log g_*$ on the spectral line shapes is rather subtle, and as a result it is typically difficult to determine accurately, so that it is a rather poor luminosity indicator in practice. Unfortunately a trigonometric parallax is not available for any of the host stars, since they were not included among the targets of the *Hipparcos* mission (Perryman et al. 1997). For planetary transits, another possible constraint is provided by the a/R_* normalized semi-major axis, which is closely related to ρ_* , the mean stellar density. The quantity a/R_* can be derived directly from the combination of

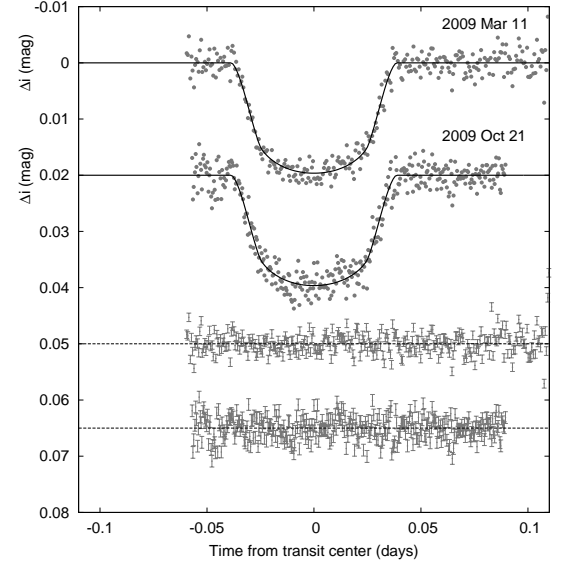


FIG. 10.— Unbinned transit light curves for HAT-P-20, acquired with KeplerCam at the FLWO 1.2 m telescope. The light curves have been EPD and TFA processed, as described in § 3.3. The dates of the events are indicated. Curves after the first are displaced vertically for clarity. Our best fit from the global modeling described in Section 3.3 is shown by the solid lines. Residuals from the fits are displayed at the bottom, in the same order as the top curves. The error bars represent the photon and background shot noise, plus the readout noise.

the transit light curves (Sozzetti et al. 2007) and the RV

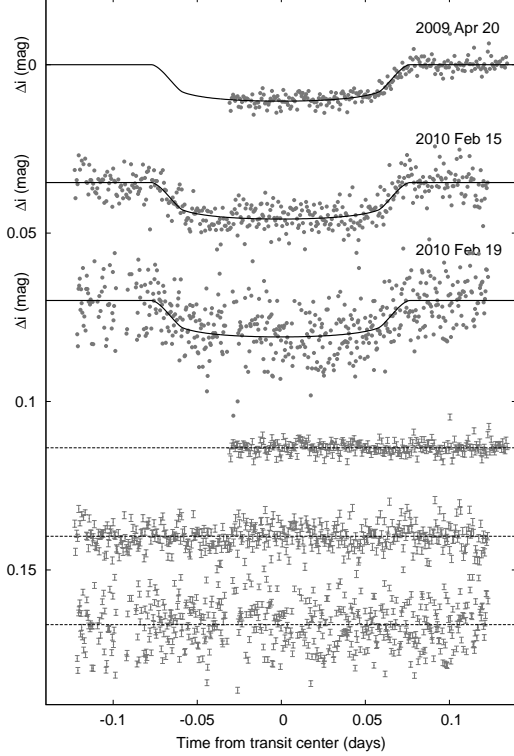


FIG. 11.— Similar to Figure 10; here we show the follow-up light curves for HAT-P-21.

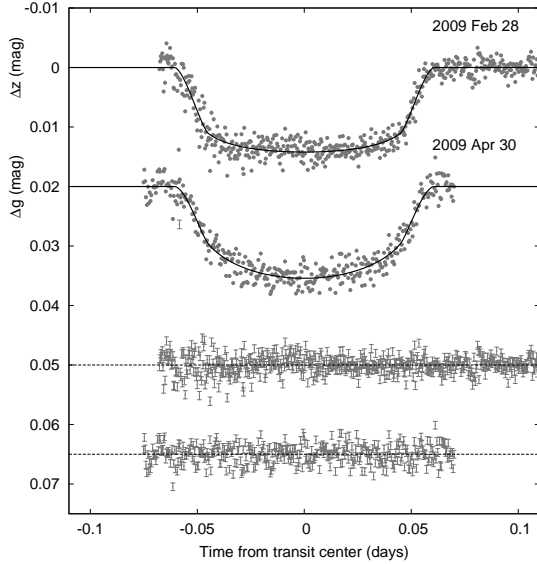


FIG. 12.— Similar to Figure 10; here we show the follow-up light curves for HAT-P-22.

data (required for eccentric cases, see Section 3.3). This, in turn, allows us to improve on the determination of the spectroscopic parameters by supplying an indirect constraint on the weakly determined spectroscopic value of $\log g_*$ that removes degeneracies. We take this approach here, as described below. The validity of our assumption, namely that the adequate physical model describing our data is a planetary transit (as opposed to a blend), is shown later in Section 3.2.

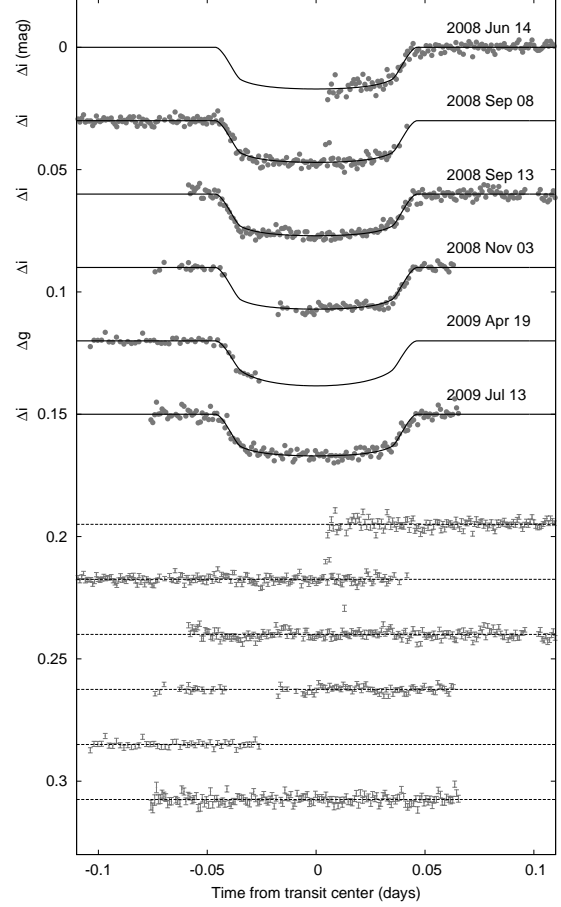


FIG. 13.— Similar to Figure 10; here we show the follow-up light curves for HAT-P-23.

TABLE 11
HIGH-PRECISION DIFFERENTIAL PHOTOMETRY OF HAT-P-23.

BJD _{UTC} (2,400,000+)	Mag ^a	σ_{Mag}	Mag(orig) ^b	Filter
54632.73784	0.02143	0.00111	10.98360	<i>i</i>
54632.73870	0.01830	0.00116	10.98170	<i>i</i>
54632.73954	0.01503	0.00115	10.97810	<i>i</i>
54632.74039	0.01859	0.00115	10.98340	<i>i</i>
54632.74125	0.01123	0.00111	10.97530	<i>i</i>
54632.74208	0.02006	0.00109	10.98390	<i>i</i>
54632.74295	0.01831	0.00111	10.98220	<i>i</i>
54632.74381	0.01766	0.00114	10.97840	<i>i</i>
54632.74637	0.02025	0.00117	10.99540	<i>i</i>
54632.74722	0.01556	0.00112	10.97990	<i>i</i>

NOTE. — Notes for this table are identical to those of Table 8.

For each system, our initial values of $T_{\text{eff}\star}$, $\log g_*$, and $[\text{Fe}/\text{H}]$ were used to determine auxiliary quantities needed in the global modeling of the follow-up photometry and radial velocities (specifically, the limb-darkening coefficients). This modeling, the details of which are described in Section 3.3, uses a Monte Carlo approach to deliver the numerical probability distribution of a/R_* and other fitted variables. For further details we refer the reader to Pál (2009b). When combining a/R_* (used as a proxy for luminosity) with assumed Gaussian distributions for $T_{\text{eff}\star}$ and $[\text{Fe}/\text{H}]$ based on the SME deter-

minations, a comparison with stellar evolution models allows the probability distributions of other stellar properties to be inferred, including $\log g_*$. Here we use the stellar evolution calculations from the Yonsei-Yale group (YY; Yi et al. 2001) for all planets presented in this work. The comparison against the model isochrones was carried out for each of 10,000 Monte Carlo trial sets for HAT-P-21, HAT-P-22, and HAT-P-23, and for 20,000 Monte Carlo trial sets for HAT-P-20 (see Section 3.3). Parameter combinations corresponding to unphysical locations in the H-R diagram (26% of the trials for HAT-P-20, and less than 1% of the trials for the other objects) were ignored, and replaced with another randomly drawn parameter set. For each system we carried out a second SME iteration in which we adopted the value of $\log g_*$ so determined and held it fixed in a new SME analysis (coupled with a new global modeling of the RV and light curves), adjusting only $T_{\text{eff}*}$, $[\text{Fe}/\text{H}]$, and $v \sin i$. This gave:

- *HAT-P-20*: $\log g_* = 4.64 \pm 0.06$, $T_{\text{eff}*} = 4595 \pm 80 \text{ K}$, $[\text{Fe}/\text{H}] = +0.35 \pm 0.08$, and $v \sin i = 2.1 \pm 0.5 \text{ km s}^{-1}$.
- *HAT-P-21*: $\log g_* = 4.31 \pm 0.06$, $T_{\text{eff}*} = 5588 \pm 80 \text{ K}$, $[\text{Fe}/\text{H}] = +0.01 \pm 0.08$, and $v \sin i = 3.5 \pm 0.5 \text{ km s}^{-1}$.
- *HAT-P-22*: $\log g_* = 4.37 \pm 0.06$, $T_{\text{eff}*} = 5302 \pm 80 \text{ K}$, $[\text{Fe}/\text{H}] = +0.24 \pm 0.08$, and $v \sin i = 0.5 \pm 0.5 \text{ km s}^{-1}$.
- *HAT-P-23*: $\log g_* = 4.33 \pm 0.06$, $T_{\text{eff}*} = 5905 \pm 80 \text{ K}$, $[\text{Fe}/\text{H}] = +0.15 \pm 0.04$, and $v \sin i = 8.1 \pm 0.5 \text{ km s}^{-1}$.

In each case the conservative uncertainties for $T_{\text{eff}*}$ and $[\text{Fe}/\text{H}]$ have been increased by a factor of two over their formal values, as before. For each system, a further iteration did not change $\log g_*$ significantly, so we adopted the values stated above as the final atmospheric properties of the stars. They are collected in Table 12.

With the adopted spectroscopic parameters the model isochrones yield the stellar mass and radius, and other properties. These are listed for each of the systems in Table 12. According to these models HAT-P-20 is a dwarf star with an estimated age of $6.7^{+5.7}_{-3.8}$ Gyr, HAT-P-21 is a slightly evolved star with an estimated age of 10.2 ± 2.5 Gyr, HAT-P-22 is a slightly evolved star with an estimated age of 12.4 ± 2.6 Gyr, and HAT-P-23 is a slightly evolved star with an estimated age of 4.0 ± 1.0 Gyr. The inferred location of each star in a diagram of a/R_* versus $T_{\text{eff}*}$, analogous to the classical H-R diagram, is shown in Figure 14. In all cases the stellar properties and their 1σ and 2σ confidence ellipsoids are displayed against the backdrop of model isochrones for a range of ages, and the appropriate stellar metallicity. For comparison, the locations implied by the initial SME results are also shown (in each case with a triangle).

The stellar evolution modeling provides color indices (see Table 12) that may be compared against the measured values as a sanity check. For each star, the best available measurements are the near-infrared magnitudes from the 2MASS Catalogue (Skrutskie et al. 2006), which are given in Table 12. These are converted to the

photometric system of the models (ESO system) using the transformations by Carpenter (2001). The resulting color indices are also shown in Table 12 for HAT-P-20 through HAT-P-23, respectively. Indeed, the colors from the stellar evolution models and from the observations agree for all of the host stars within 2σ . The distance to each object may be computed from the absolute K magnitude from the models and the 2MASS K_s magnitudes, which has the advantage of being less affected by extinction than optical magnitudes. The results are given in Table 12, where in all cases the uncertainty excludes possible systematics in the model isochrones that are difficult to quantify.

3.2. Excluding blend scenarios

Our initial spectroscopic analyses discussed in Section 2.2 and Section 2.3 rule out the most obvious astrophysical false positive scenarios. However, more subtle phenomena such as blends (contamination by an unresolved eclipsing binary, whether in the background or associated with the target) can still mimic both the photometric and spectroscopic signatures we see. In the following section we investigate whether such scenarios may have caused the observed photometric and spectroscopic features.

3.2.1. Spectral line-bisector analysis

Following Torres et al. (2007), we explored the possibility that the measured radial velocities are not real, but are instead caused by distortions in the spectral line profiles due to contamination from a nearby unresolved eclipsing binary. A bisector span (BS) analysis for each system based on the Keck spectra was done as described in §5 of Bakos et al. (2007). In general, none of the Keck/HIRES spectra suffer significant sky contamination. Nevertheless, we calculated the Sky Contamination Factors (SCF) as described in Hartman et al. (2009), and corrected for the minor correlation between SCF and BS. The results are exhibited in Figure 15, where we show the SCF-BS and RV-BS_{SCF} (BS after SCF correction) plots for each planetary system. We also calculated the Spearman rank-order correlation coefficients (denoted as R_s for the RV vs. BS quantities and the false alarm probabilities (see Table 13). There is no correlation for HAT-P-21, HAT-P-22 and HAT-P-23, and thus the interpretation of these systems as transiting planets is clear. There is an anti-correlation present for HAT-P-20, which is strengthened when the SCF correction is applied. A plausible explanation for this is that the neighboring star at $6''$ separation (see Figure 5) is bleeding into the slit, even though we were careful during the observations to keep the slit centered on the main target, and adjusted the slit orientation to be perpendicular to the direction to the neighbor. We simulated this scenario, and calculated the expected BS as a function of RV due to the neighbor, assuming that the two stars have the same systemic velocity and the seeing is $1''$. Indeed, we get a slight anti-correlation from this simulation, and the range of magnitude in the BS variation is consistent with the observations. It is also possible that some of the anti-correlation is due to the fact that the slit was not in vertical angle for many of the observations. The non-vertical slit mode may result

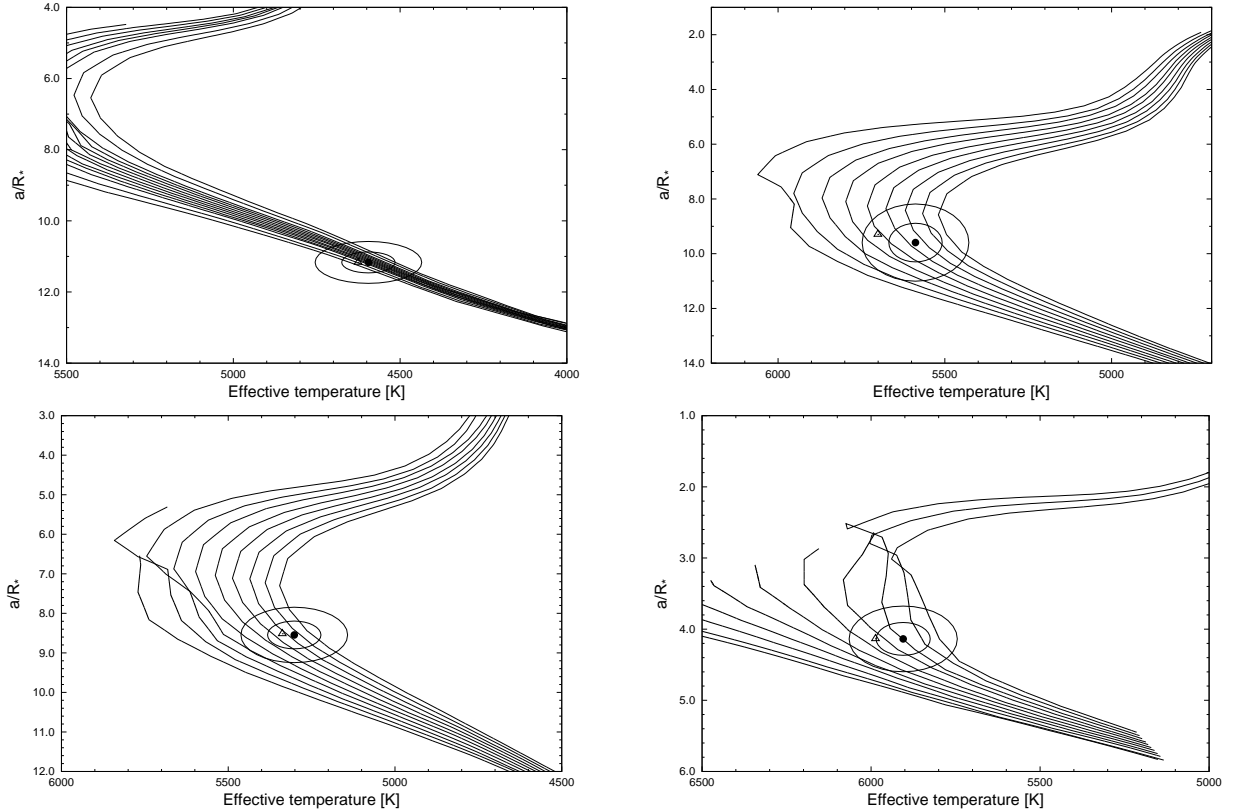


FIG. 14.— Upper left: Model isochrones from Yi et al. (2001) for the measured metallicity of HAT-P-20, $[\text{Fe}/\text{H}] = +0.35$, and ages of 3.0, 4.0, 5.0, 5.5, 6.0, 6.5, 7.0, 7.5, 8.0, 8.5, 9.0, 10.0 and 11.0 Gyr (left to right). The adopted values of $T_{\text{eff}\star}$ and a/R_\star are shown together with their 1σ and 2σ confidence ellipsoids. The initial values of $T_{\text{eff}\star}$ and a/R_\star from the first SME and light curve analyses are represented with a triangle. Upper right: Same as upper left, here we show the results for HAT-P-21, with $[\text{Fe}/\text{H}] = +0.01$, and ages of 5.0, 6.0, 7.0, 8.0, 9.0, 10.0, 11.0, 12.0, and 13.0 Gyr (left to right). Lower left: Same as upper left, here we show the results for HAT-P-22, with $[\text{Fe}/\text{H}] = +0.24$, and ages of 5.0, 6.0, 7.0, 8.0, 9.0, 10., 11.0, 12., 13.0, and 14.0 Gyr (left to right). Lower right: Same as upper left, here we show the results for HAT-P-23, with $[\text{Fe}/\text{H}] = +0.15$, and ages of 0.2, 0.5, 1.0, 1.5, 2.0, 2.5, 3.0, 3.5, 4.0, 4.5 and 5.0 Gyr (left to right).

in wavelength-dependent slit losses due to atmospheric dispersion, and this could bring in a correlation with the sky background, and change the shape of the spectral lines.

3.3. Global modeling of the data

This section describes the procedure we followed for each system to model the HATNet photometry, the follow-up photometry, and the radial velocities simultaneously. Our model for the follow-up light curves used analytic formulae based on Mandel & Agol (2002) for the eclipse of a star by a planet, with limb darkening being prescribed by a quadratic law. The limb darkening coefficients for the Sloan g band, Sloan i band, and Sloan z band were interpolated from the tables by Claret (2004) for the spectroscopic parameters of each star as determined from the SME analysis (Section 3.1). The transit shape was parametrized by the normalized planetary radius $p \equiv R_p/R_\star$, the square of the impact parameter b^2 , and the reciprocal of the half duration of the transit ζ/R_\star . We chose these parameters because of their simple geometric meanings and the fact that these show negligible correlations (see Bakos et al. 2010). The relation between ζ/R_\star and the quantity a/R_\star , used in Section 3.1, is given by

$$a/R_\star = P/2\pi(\zeta/R_\star)\sqrt{1-b^2}\sqrt{1-e^2}/(1+e\sin\omega) \quad (1)$$

(see, e.g., Tingley & Sackett 2005). Note the subtle dependency of a/R_\star on the $k \equiv e\cos\omega$ and $h \equiv e\sin\omega$ Lagrangian orbital parameters that are typically derived from the RV data (ω is the longitude of periastron). This dependency is often ignored in the literature, and a/R_\star is quoted as a “pure” light curve parameter. Of course, if high quality secondary eclipse observations are available that determine both the location and duration of the occultation, then k and h can be determined without RV data. Our model for the HATNet data was the simplified “P1P3” version of the Mandel & Agol (2002) analytic functions (an expansion in terms of Legendre polynomials), for the reasons described in Bakos et al. (2010). Following the formalism presented by Pál (2009), the RVs were fitted with an eccentric Keplerian model parametrized by the semi-amplitude K and Lagrangian elements k and h . Note that we allowed for an eccentric orbit for all planets, even if the results were consistent with a circular orbit. There are several reasons for this: i) many of the close-in hot Jupiters show eccentric orbits, thus the assumption of fixing $e = 0$ has no physical justification (while this has been customary in early discoveries relying on very few data-points) ii) the error-bars on various other derived quantities (including a/R_\star) are more realistic with the inclusion of eccentricity, and iii) non-zero eccentricities can be very important in proper interpretation of these systems.

We assumed that there is a strict periodicity in the

TABLE 12
STELLAR PARAMETERS FOR HAT-P-20–HAT-P-23

Parameter	HAT-P-20	HAT-P-21	HAT-P-22	HAT-P-23	Source
Spectroscopic properties					
$T_{\text{eff}\star}$ (K)	4595 ± 80	5588 ± 80	5302 ± 80	5905 ± 80	SME ^a
[Fe/H]	$+0.35 \pm 0.08$	$+0.01 \pm 0.08$	$+0.24 \pm 0.08$	$+0.15 \pm 0.04$	SME
$v \sin i$ (km s ^{−1}) . . .	2.1 ± 0.5	3.5 ± 0.5	0.5 ± 0.5	8.1 ± 0.5	SME
v_{mac} (km s ^{−1}) . . .	2.21	3.74	3.30	4.22	SME
v_{mic} (km s ^{−1}) . . .	0.85	0.85	0.85	0.85	SME
γ_{RV} (km s ^{−1})	-18.81 ± 0.68	-53.19 ± 0.09	$+12.49 \pm 0.28$	-15.10 ± 0.30	DS
Photometric properties					
V (mag)	11.339	11.685	9.732	12.432	TASS
$V - I_C$ (mag)	1.50 ± 0.12	0.654 ± 0.097	0.992 ± 0.066	0.68 ± 0.12	TASS
J (mag)	9.276 ± 0.022	10.503 ± 0.022	8.293 ± 0.023	11.103 ± 0.022	2MASS
H (mag)	8.743 ± 0.021	10.154 ± 0.019	7.935 ± 0.029	10.846 ± 0.022	2MASS
K_s (mag)	8.601 ± 0.019	10.111 ± 0.018	7.837 ± 0.021	10.791 ± 0.020	2MASS
$J - K$ (mag,ESO) . . .	0.715 ± 0.033	0.419 ± 0.031	0.486 ± 0.034	0.335 ± 0.032	2MASS
Derived properties					
M_\star (M_\odot)	0.756 ± 0.028	0.947 ± 0.042	0.916 ± 0.035	1.130 ± 0.035	YY+ a/R_\star +SME ^b
R_\star (R_\odot)	0.694 ± 0.021	1.105 ± 0.083	1.040 ± 0.044	1.203 ± 0.074	YY+ a/R_\star +SME
$\log g_\star$ (cgs)	4.63 ± 0.02	4.33 ± 0.06	4.36 ± 0.04	4.33 ± 0.05	YY+ a/R_\star +SME
L_\star (L_\odot)	0.19 ± 0.02	$1.06^{+0.20}_{-0.16}$	0.77 ± 0.09	1.58 ± 0.23	YY+ a/R_\star +SME
M_V (mag)	7.07 ± 0.17	4.80 ± 0.19	5.22 ± 0.14	4.31 ± 0.16	YY+ a/R_\star +SME
M_K (mag,ESO)	4.42 ± 0.09	3.12 ± 0.16	3.30 ± 0.10	2.86 ± 0.14	YY+ a/R_\star +SME
$J - K$ (mag,ESO)	0.66 ± 0.02	0.44 ± 0.02	0.50 ± 0.02	0.37 ± 0.01	YY+ a/R_\star +SME
Age (Gyr)	$6.7^{+5.7}_{-3.8}$	10.2 ± 2.5	12.4 ± 2.6	4.0 ± 1.0	YY+ a/R_\star +SME
Distance (pc)	70 ± 3	254 ± 19	82 ± 3	393 ± 25	YY+ a/R_\star +SME

^a SME = “Spectroscopy Made Easy” package for the analysis of high-resolution spectra (Valenti & Piskunov 1996). These parameters rely primarily on SME, but have a small dependence also on the iterative analysis incorporating the isochrone search and global modeling of the data, as described in the text.

^b YY+ a/R_\star +SME = Based on the YY isochrones (Yi et al. 2001), a/R_\star as a luminosity indicator, and the SME results.

TABLE 13
SUMMARY OF RV VS. BS CORRELATIONS.

Name	R_{s1} ^a	FAP ₁ ^b	R_{s2} ^c	FAP ₂ ^d
HAT-P-20	-0.73	2.46%	-0.92	0.05%
HAT-P-21	-0.24	39%	-0.20	47%
HAT-P-22	0.33	30%	0.27	37%
HAT-P-23	0.27	37%	0.27	37%

^a The Spearman correlation coefficient between the bisector (BS) variations and the radial velocities (RV).

^b False alarm probability for R_{s1} .

^c The Spearman correlation coefficient between BS corrected for the sky contamination factor (SCF) and the RVs.

^d False alarm probability for R_{s2} .

individual transit times. For each system we assigned the transit number $N_{tr} = 0$ to a complete follow-up light curve. For HAT-P-20b this was the light curve gathered on 2009 Oct 21, for HAT-P-21b: 2010 Feb 19, HAT-P-22b: 2009 Feb 28, and HAT-P-23b: 2008 Sep 13. The adjustable parameters in the fit that determine the ephemeris were chosen to be the time of the first transit center observed with HATNet ($T_{c,-252}$, $T_{c,-286}$, $T_{c,-135}$, and $T_{c,-312}$ for HAT-P-20b through HAT-P-23b respectively) and that of the last transit center observed with the FLWO 1.2m telescope ($T_{c,0}$, $T_{c,1}$, $T_{c,19}$, and $T_{c,250}$ for HAT-P-20b through HAT-P-23b respectively). We used these as opposed to period and reference epoch in order to minimize correlations between parameters (see Pál et al. 2008). Times of mid-transit for intermediate events were interpolated using these two epochs and the

corresponding transit number of each event, N_{tr} . The eight main parameters describing the physical model for each system were thus the first and last transit center times, R_p/R_\star , b^2 , ζ/R_\star , K , $k \equiv e \cos \omega$, and $h \equiv e \sin \omega$. For HAT-P-20b, HAT-P-22b, and HAT-P-23b three additional parameters were included (for each system) that have to do with the instrumental configuration (blend factor, out-of-transit magnitudes, gamma velocities; see later). For HAT-P-21b seven additional parameters were included, because it was observed in 3 different HATNet fields. These are the HATNet blend factor B_{inst} (one for each HATNet field), which accounts for possible dilution of the transit in the HATNet light curve from background stars due to the broad PSF (20'' FWHM), the HATNet out-of-transit magnitude $M_{0,\text{HATNet}}$ (one for each HATNet field), and the relative zero-point γ_{rel} of the Keck RVs.

We extended our physical model with an instrumental model that describes brightness variations caused by systematic errors in the measurements. This was done in a similar fashion to the analysis presented by Bakos et al. (2010). The HATNet photometry has already been EPD- and TFA-corrected before the global modeling, so we only considered corrections for systematics in the follow-up light curves. We chose the “ELTG” method, i.e., EPD was performed in “local” mode with EPD coefficients defined for each night, and TFA was performed in “global” mode using the same set of stars and TFA coefficients for all nights. The five EPD parameters were the hour angle (representing a monotonic trend that changes linearly over time), the square of the hour angle (reflecting elevation), and the stellar profile parameters (equiv-

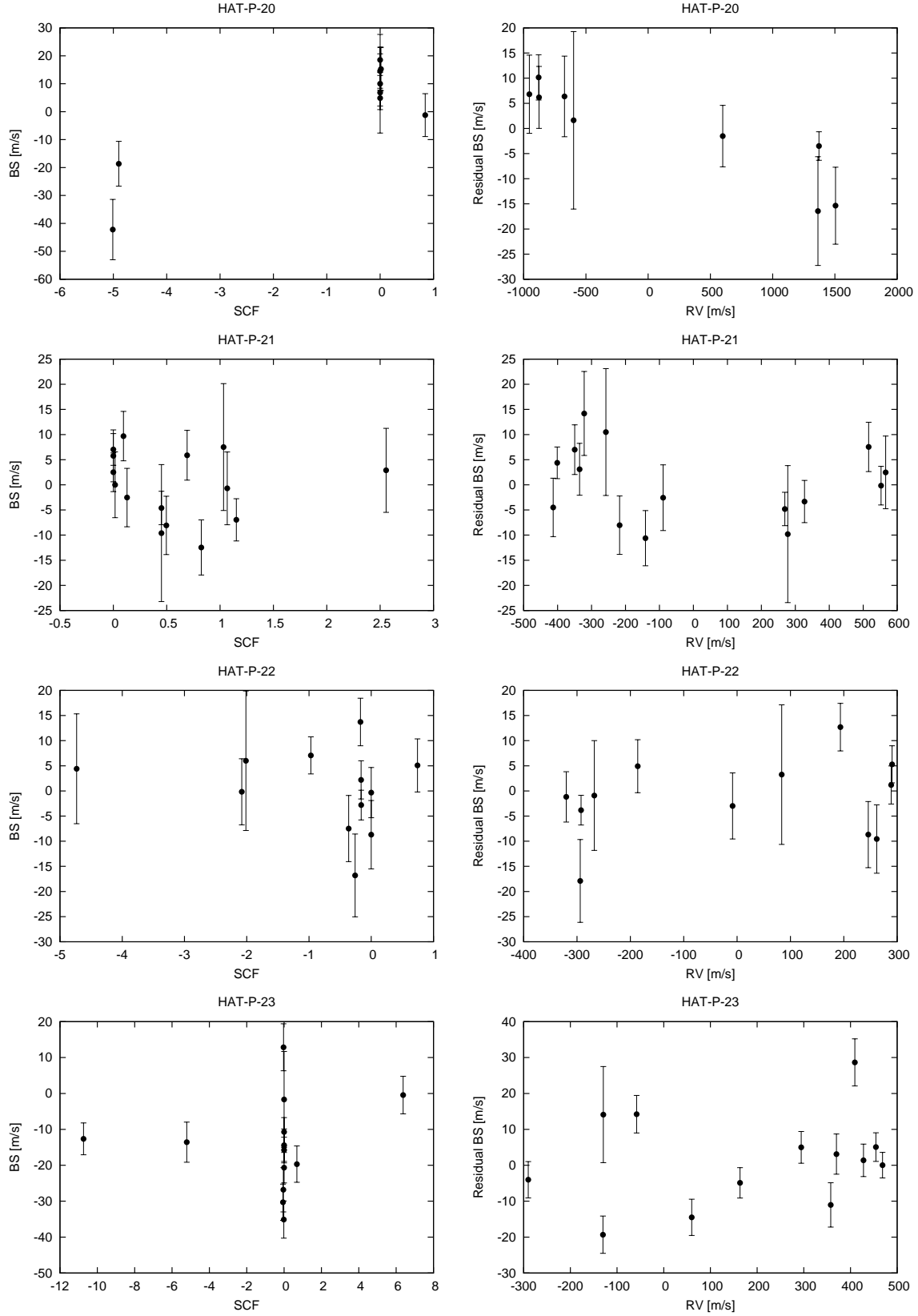


FIG. 15.— Panels on the left show the bisector spans (BS) as a function of Sky Contamination Factor (SCF). Panels on the right exhibit the SCF-corrected BS as a function of the radial velocities. The individual planets are labeled.

alent to FWHM, elongation, and position angle of the image). The functional forms of the above parameters

contained six coefficients, including the auxiliary out-of-transit magnitude of the individual events. For each sys-

tem the EPD parameters were independent for all nights, implying 12, 18, 12, and 36 additional coefficients in the global fit for HAT-P-20b through HAT-P-23b respectively. For the global TFA analysis we chose 20, 3, 10, and 20 template stars for HAT-P-20b through HAT-P-23b that had good quality measurements for all nights and on all frames, implying an additional 20, 3, 10, and 20 parameters in the fit for each system. In all cases the total number of fitted parameters (43, 36, 33 and 67 for HAT-P-20b through HAT-P-23b) was much smaller than the number of data points (755, 1172, 892 and 953, counting only RV measurements and follow-up photometry measurements).

The joint fit was performed as described in Bakos et al. (2010). We minimized χ^2 in the space of parameters by using a hybrid algorithm, combining the downhill simplex method (AMOEBA; see Press et al. 1992) with a classical linear least squares algorithm. Uncertainties for the parameters were derived by applying the Markov Chain Monte-Carlo method (MCMC, see Ford 2006). This provided the full *a posteriori* probability distributions of all adjusted variables. The *a priori* distributions of the parameters for these chains were chosen to be Gaussian, with eigenvalues and eigenvectors derived from the Fisher covariance matrix for the best-fit solution. The Fisher covariance matrix was calculated analytically using the partial derivatives given by Pál (2009).

Following this procedure we obtained the *a posteriori* distributions for all fitted variables, and other quantities of interest such as a/R_* . As described in Section 3.1, a/R_* was used together with stellar evolution models to infer a value for $\log g_*$ that is significantly more accurate than the spectroscopic value. The improved estimate was in turn applied to a second iteration of the SME analysis, as explained previously, in order to obtain better estimates of $T_{\text{eff},*}$ and $[\text{Fe}/\text{H}]$. The global modeling was then repeated with updated limb-darkening coefficients based on those new spectroscopic determinations. The resulting geometric parameters pertaining to the light curves and velocity curves for each system are listed in Table 14.

Included in each table is the RV “jitter”, which is a noise term that we added in quadrature to the internal errors for the RVs in order to achieve $\chi^2/\text{dof} = 1$ from the RV data for the global fit. The jitter is a combination of assumed astrophysical noise intrinsic to the star, plus instrumental noise rising from uncorrected instrumental effects (such as a template spectrum taken under sub-optimal conditions).

The planetary parameters and their uncertainties were derived by combining the *a posteriori* distributions for the stellar, light curve, and RV parameters. In this way we find masses and radii for each planet. These and other planetary parameters are listed at the bottom of Table 14, and further discussed in § 4.

4. DISCUSSION

4.1. HAT-P-20b

HAT-P-20b is a very massive ($M_p = 7.246 \pm 0.187 M_J = 2302.9 \pm 59.5 M_\oplus$) and very compact ($R_p = 0.867 \pm 0.033 R_J$) hot Jupiter orbiting a K3 (Skiff 2009) star. HAT-P-20b is the sixth most massive, and second most dense transiting planet with

$\rho_p = 13.78 \pm 1.50 \text{ g cm}^{-3}$ (see Figure 16). The only planet (or brown dwarf) denser than HAT-P-20b is CoRoT-3b (Deleuil et al. 2008) with $\rho_p \approx 27 \text{ g cm}^{-3}$. Modeling HAT-P-20b may be a challenge, as the oldest (4 Gyr, i.e. yielding the most compact planets) Fortney et al. (2007) models with $M_p = 2154 M_\oplus$ total mass and $100 M_\oplus$ core-mass predict a much bigger radius ($1.04 R_J$). The observed radius of $0.87 M_J$ would require a very high metal content. We note that the host star is one of the most metal rich stars that have a transiting planet ($[\text{Fe}/\text{H}] = +0.35 \pm 0.08$). Curiously, HAT-P-20b orbits a fairly late type star (K3), as compared to most of the massive hot Jupiters that orbit $\sim \text{F5}$ dwarfs. It is also different from the rest of the population in that the orbit is consistent with circular at the 3σ level. The irradiation HAT-P-20b receives is one of the smallest, clearly making it a pL class exoplanet (Fortney et al. 2008): $\langle F \rangle = (2.00 \pm 0.19) \cdot 10^8 \text{ erg s}^{-1} \text{ cm}^{-2}$, comparable to the mean flux per orbit for another “heavy” planet HD 17156b on a 21 d period orbit. The only other massive planet that receives less average flux (integrated over an orbit) is HD 80606b. HAT-P-20 is an extreme outlier in the M_p – M_* plane; it is a relatively small mass star harboring a very massive planet. Another outlier (albeit to a much lesser extent) with similar planetary radius and stellar mass is WASP-10b (Johnson et al. 2009; Christian et al. 2009), but this planet has less than half of the mass of HAT-P-20b ($3.09 M_J$). We also calculated the maximum mass of a stable moon for both the prograde and retrograde cases, and derived $0.128 M_\oplus$ and $8.31 M_\oplus$, respectively, i.e. HAT-P-20b can harbor a fairly massive moon. An $8.31 M_\oplus$ retrograde moon would cause $\sim 10 \text{ s}$ variations in the transit times, which is marginally detectable from the ground.

HAT-P-20 has a close-by faint and red companion star at $\sim 6.86''$ separation. Based on the Palomar sky survey archival plates, we confirm that they form a close common-proper motion pair, thus it is very likely that the two stars are physically associated. The binary has appeared in the Washington Double Star compilation (WDS) as POU2795, and was discovered by Pourteau (1933). Furthermore, based on the summary of observations in the WDS, there is already a hint of orbital motion of the companion to HAT-P-20 over the last century. The position angle of the companion changed from $\text{PA}=323^\circ$ to $\text{PA}=320^\circ$ over the course of 89 years (between 1909 and 1998), and it seems to be retrograde on the sky (clockwise). Thus, HAT-P-20 is yet another example of a massive planet in a binary system (Udry et al. 2002). The binary companion makes this system ideal for high precision ground or space-based studies, as it provides a natural comparison source, even though it has a later spectral type.

4.2. HAT-P-21b

With a mass of $M_p = 4.063 \pm 0.161 M_J$, HAT-P-21b is the 11th most massive transiting planet. HAT-P-21b has a radius of $R_p = 1.024 \pm 0.092 R_J$, mean density $\rho_p = 4.68_{-0.99}^{+1.59} \text{ g cm}^{-3}$, and orbits on a moderately eccentric orbit with $e = 0.228 \pm 0.016$, $\omega = 309 \pm 3^\circ$. The transits occur near apastron. As noted by Buchhave et al. (2010), $4 M_J$ mass planets are very rare in the sample of currently known transiting exoplanets, and the only sib-

TABLE 14
ORBITAL AND PLANETARY PARAMETERS FOR HAT-P-20b–HAT-P-23b

Parameter	HAT-P-20b	HAT-P-21b	HAT-P-22b	HAT-P-23b
Light curve parameters				
P (days)	2.875317 ± 0.000004	4.124481 ± 0.000007	3.212220 ± 0.000009	1.212884 ± 0.000002
T_c (BJD _{UTC}) ^a	$2455080.92661 \pm 0.00021$	$2454996.41312 \pm 0.00069$	$2454930.22001 \pm 0.00025$	$2454852.26464 \pm 0.00018$
T_{14} (days) ^a	0.0770 ± 0.0008	0.1530 ± 0.0027	0.1196 ± 0.0014	0.0908 ± 0.0007
$T_{12} = T_{34}$ (days) ^a	0.0137 ± 0.0009	0.0184 ± 0.0029	0.0144 ± 0.0013	0.0105 ± 0.0007
a/R_\star	11.17 ± 0.29	9.60 ± 0.71	8.55 ± 0.35	4.14 ± 0.23
ζ/R_\star	31.32 ± 0.22	14.81 ± 0.15	18.97 ± 0.09	24.90 ± 0.12
R_p/R_\star	0.1284 ± 0.0016	0.0950 ± 0.0022	0.1065 ± 0.0017	0.1169 ± 0.0012
b^2	$0.398^{+0.032}_{-0.034}$	$0.298^{+0.089}_{-0.118}$	$0.217^{+0.052}_{-0.065}$	$0.105^{+0.053}_{-0.049}$
$b \equiv a \cos i/R_\star$	$0.631^{+0.025}_{-0.028}$	$0.546^{+0.074}_{-0.139}$	$0.466^{+0.052}_{-0.083}$	$0.324^{+0.070}_{-0.101}$
i (deg)	86.8 ± 0.2	87.2 ± 0.7	$86.9^{+0.6}_{-0.5}$	85.1 ± 1.5
Limb-darkening coefficients ^b				
a_i (linear term)	0.4719	0.2976	0.3587	0.2524
b_i (quadratic term)	0.2174	0.3131	0.2831	0.3426
a_g	0.7080	0.5311
b_g	0.1165	0.2539
RV parameters				
K (m s ⁻¹)	1246.0 ± 8.1	548.3 ± 14.2	313.3 ± 4.2	368.5 ± 17.6
k_{RV}^c	0.012 ± 0.004	0.147 ± 0.011	-0.008 ± 0.008	-0.048 ± 0.023
h_{RV}^c	-0.007 ± 0.008	-0.175 ± 0.019	0.004 ± 0.016	0.090 ± 0.052
e	0.015 ± 0.005	0.228 ± 0.016	0.016 ± 0.009	0.106 ± 0.044
ω (deg)	317 ± 130	309 ± 3	156 ± 66	118 ± 25
RV jitter (m s ⁻¹)	15.7	26.4	9.9	34.7
Secondary eclipse parameters (derived)				
T_s (BJD _{UTC})	2455082.385 ± 0.007	2454998.865 ± 0.029	2454931.809 ± 0.016	2454852.834 ± 0.018
$T_{s,14}$	0.0764 ± 0.0010	0.1163 ± 0.0068	0.1204 ± 0.0032	0.1064 ± 0.0095
$T_{s,12}$	0.0134 ± 0.0009	0.0117 ± 0.0015	0.0145 ± 0.0014	0.0129 ± 0.0020
Planetary parameters				
M_p (M_J)	7.246 ± 0.187	4.063 ± 0.161	2.147 ± 0.061	2.090 ± 0.111
R_p (R_J)	0.867 ± 0.033	1.024 ± 0.092	1.080 ± 0.058	1.368 ± 0.090
$C(M_p, R_p)^d$	0.50	0.28	0.36	0.56
ρ_p (g cm ⁻³)	13.78 ± 1.50	$4.68^{+1.59}_{-0.99}$	$2.11^{+0.40}_{-0.29}$	1.01 ± 0.18
$\log g_p$ (cgs)	4.38 ± 0.03	3.98 ± 0.08	3.66 ± 0.05	3.44 ± 0.05
a (AU)	0.0361 ± 0.0005	0.0494 ± 0.0007	0.0414 ± 0.0005	0.0232 ± 0.0002
T_{eq} (K)	970 ± 23	1283 ± 50	1283 ± 32	2056 ± 66
Θ^e	0.794 ± 0.031	0.413 ± 0.038	0.179 ± 0.010	0.062 ± 0.004
F_{per} (10 ⁸ erg s ⁻¹ cm ⁻²) ^f	2.06 ± 0.20	10.0 ± 1.5	6.33 ± 0.67	50.0 ± 11.4
F_{ap} (10 ⁸ erg s ⁻¹ cm ⁻²) ^f	1.94 ± 0.19	3.96 ± 0.66	5.91 ± 0.60	32.7 ± 2.7
$\langle F \rangle$ (10 ⁸ erg s ⁻¹ cm ⁻²) ^f	2.00 ± 0.19	6.12 ± 0.97	6.12 ± 0.62	40.3 ± 5.3

^a T_c : Reference epoch of mid transit that minimizes the correlation with the orbital period. It corresponds to $N_{tr} = -16$. BJD is calculated from UTC. T_{14} : total transit duration, time between first to last contact; $T_{12} = T_{34}$: ingress/egress time, time between first and second, or third and fourth contact.

^b Values for a quadratic law, adopted from the tabulations by Claret (2004) according to the spectroscopic (SME) parameters listed in Table 12.

^c Lagrangian orbital parameters derived from the global modeling, and primarily determined by the RV data.

^d Correlation coefficient between the planetary mass M_p and radius R_p .

^e The Safronov number is given by $\Theta = \frac{1}{2}(V_{esc}/V_{orb})^2 = (a/R_p)(M_p/M_\star)$ (see Hansen & Barman 2007).

^f Incoming flux per unit surface area. $\langle F \rangle$ is averaged over the orbit.

lings of HAT-P-21b are HD 80606b (4.08 M_J ; Naef et al. 2001) and HAT-P-16b (4.19 M_J ; Buchhave et al. 2010). Among these, HAT-P-16b has a shorter period, also an eccentric orbit, and a much larger radius (1.29 R_J). HD 80606b, on the other hand, has a similar radius, and orbits on an extremely eccentric ($e = 0.93$) orbit at 111 day period. It appears that HAT-P-21b is thus an unusual, short period, eccentric, massive and compact planet.

The only models from Fortney et al. (2007) consistent with the observed radius are 4 Gyr models with 100 M_\oplus core mass, yielding 1.05 R_J radius. Probably HAT-P-21b has an even higher metal content. HAT-P-21b has a very high mean density; it is 8th among all TEPs, and very similar to HD 80606b and WASP-14b.

The flux received by the planet varies between $(10.0 \pm 1.5) \cdot 10^8 \text{ erg s}^{-1} \text{ cm}^{-2}$ and $(3.96 \pm 0.66) \cdot 10^8 \text{ erg s}^{-1} \text{ cm}^{-2}$. Interestingly, this puts HAT-P-21b on the borderline between pL (low irradiation) and pM (high irradiation) planets. At the time of occultation, HAT-P-21b is just approaching its periastron, thus entering the irradiation level quoted for pM type planets.

4.3. HAT-P-22b

HAT-P-22b has a mass of $M_p = 2.147 \pm 0.061 M_J$, radius of $R_p = 1.080 \pm 0.058 R_J$, and mean density of $\rho_p = 2.11^{+0.40}_{-0.29} \text{ g cm}^{-3}$. HAT-P-22b orbits a fairly metal rich ($[\text{Fe}/\text{H}] = +0.24 \pm 0.08$), bright ($V=9.732$), and close-by ($82 \pm 3 \text{ pc}$) star. Similarly to HAT-P-20, the host star has a faint and red neighbor at $9''$ separation

that is co-moving with HAT-P-22 (based on the POSS plates and recent Keck/HIRES snapshots), thus they are likely to form a physical pair.

HAT-P-22b belongs to the moderately massive ($\sim 2 M_J$) and compact ($R_p \approx 1 R_J$) hot Jupiters, such as HAT-P-15b ($M_p=1.95 M_J$, $R_p=1.07 R_J$; Kovács et al. 2010), HAT-P-14b ($M_p=2.23 M_J$, $R_p=1.15 R_J$; Torres et al. 2010), and WASP-8b ($M_p=2.25 M_J$, $R_p=1.05 R_J$; Queloz et al. 2010). The radius distribution is almost bi-modal for these planets (see Figure 16), with members of the inflated ($R_p \approx 1.3 R_J$) group being: HAT-P-23b ($M_p=2.09 M_J$, $R_p=1.37 R_J$; this work), Kepler-5b ($M_p=2.10 M_J$, $R_p=1.31 R_J$; Kipping & Bakos 2010; Koch et al. 2010), CoRoT-11b ($M_p=2.33 M_J$, $R_p=1.43 R_J$; Gandolfi 2010).

HAT-P-22b is broadly consistent with the models of Fortney et al. (2008). For 300 Myr, 1 Gyr and 4 Gyr models it requires a $100 M_\oplus$, $50 M_\oplus$ and $25 M_\oplus$ core, respectively, to have a radius of $\sim 1.08 R_J$. The low incoming flux (see Table 14) means that HAT-P-22b is a pL class planet. HAT-P-22b can harbor a $0.96 M_\oplus$ mass retrograde moon, which would cause transit timing variations (TTVs) of ~ 2 seconds.

4.4. HAT-P-23b

HAT-P-23b belongs to the inflated group of $2 M_J$ planets (see discussion above for HAT-P-22b). This planet has a mass of $M_p = 2.090 \pm 0.111 M_J$, radius $R_p = 1.368 \pm 0.090 R_J$, and mean density $\rho_p = 1.01 \pm 0.18 \text{ g cm}^{-3}$. The orbit is nearly circular, with the eccentricity being marginally significant. The reason for the somewhat higher than usual errors in the RV parameters is the high jitter of the star (34.7 m s^{-1}), which may be related to the moderately high $v \sin i = 8.1 \pm 0.5 \text{ km s}^{-1}$ and the very close-in orbit of HAT-P-23b. The Fortney et al. (2008) models can not reproduce the observed radius of HAT-P-23b; even for the youngest, (300 Myr) core-less models, the theoretical radius for its mass is $1.25 R_J$. HAT-P-23b orbits its host star on a very close-in orbit. The orbital period is only 1.2129 days; almost identical to that of OGLE-TR-56b (1.21192 days). The nominal planetary radius of the two objects is also the same within 1%, but OGLE-TR-56b is much less massive ($1.39 M_J$). The flux falling on HAT-P-23b from its host star is one of the highest (i.e. belongs to the pM class objects), and is similar to that of HAT-P-7b and OGLE-TR-56b. We also calculated the spiral in-fall timescale for each new discovery based on Levrard, Winisdoerffer, & Chabrier (2009) and Dobbs-Dixon et al. (2004). By assuming that the stellar dissipation factor is $Q_\star = 10^6$, the infall time for HAT-P-23b is $\tau_{infall} = 7.5^{+2.9}_{-1.8} \text{ Myr}$, one of the shortest among exoplanets.

The Rossiter-McLaughlin effect for HAT-P-23b should be quite significant, given the moderately high $v \sin i = 8.1 \pm 0.5 \text{ km s}^{-1}$ of the host star, and the $\Delta i = 17 \text{ mmag}$ deep transit. The impact parameter is also “ideal” ($b = 0.324^{+0.070}_{-0.101}$), i.e. it is not equatorial ($b = 0$), where there would be a strong degeneracy between the stellar rotational velocity $v \sin i$ and the sky-projected angle of the stellar spin axis and the orbital normal, λ , and

is also far from grazing, where the transit is short, and other system parameters have lower accuracy. The effective temperature of the star ($T_{\text{eff}\star} = 5905 \pm 80 \text{ K}$) is close to the critical temperature of 6250 K noted recently by Winn et al. (2010), which may be a border-line between systems where the stellar spin axes and planetary orbital normals are preferentially aligned ($T_{\text{eff}\star} < 6250 \text{ K}$) and those that are misaligned ($T_{\text{eff}\star} > 6250 \text{ K}$). An alternative hypothesis has been brought up by Schlaufman (2010), where misaligned stellar spin axes and orbital normals are related to the mass of the host star. The mass of HAT-P-23 (1.13 ± 0.04) is sufficiently close to the suggested dividing line of $M_\star = 1.2 M_\odot$, thus it will provide an excellent additional test for these ideas.

4.5. Summary

We presented the discovery of four new massive transiting planets, and provided accurate characterization of the host star and planetary parameters. These 4 new systems are very diverse, and significantly expand the sample of ~ 13 other massive ($M_p \gtrsim 2 M_J$) planets. Two of the new discoveries orbit stars that have fainter, most probably physically associated companions. The new discoveries do not tend to enhance the mass–eccentricity correlation, since only one (HAT-P-21b) is significantly eccentric. Also, the tentative mass– $v \sin i$ correlation noted in the Introduction is weakened by the new discoveries. The heavier mass planets (HAT-P-20b and HAT-P-21b) seem to be inconsistent with current theoretical models in that they are too dense, and would require a huge core (or metal content) to have such small radii. One planet (HAT-P-23b) is also inconsistent with the models (unless we assume that the planet is very young), but in the opposite sense; it has an inflated radius. It has been noted by Winn et al. (2010) and Schlaufman (2010) that systems exhibiting stellar spin axis–planetary orbital normal misalignment are preferentially eccentric and heavy mass planets (in addition to the key parameter being the effective temperature or mass of the host star, respectively). The four new planets presented in this work will provide additional important tests for checking these conjectures. The host stars are all bright ($9.7 < V < 12.4$), and thus enable in-depth future characterization of these systems.

HATNet operations have been funded by NASA grants NNG04GN74G, NNX08AF23G and SAO IR&D grants. Work of G.Á.B. and J. Johnson were supported by the Postdoctoral Fellowship of the NSF Astronomy and Astrophysics Program (AST-0702843 and AST-0702821, respectively). GT acknowledges partial support from NASA grant NNX09AF59G. We acknowledge partial support also from the Kepler Mission under NASA Cooperative Agreement NCC2-1390 (D.W.L., PI). G.K. thanks the Hungarian Scientific Research Foundation (OTKA) for support through grant K-81373. This research has made use of Keck telescope time granted through NOAO and NASA, and uses observations obtained with facilities of the Las Cumbres Observatory Global Telescope.

REFERENCES

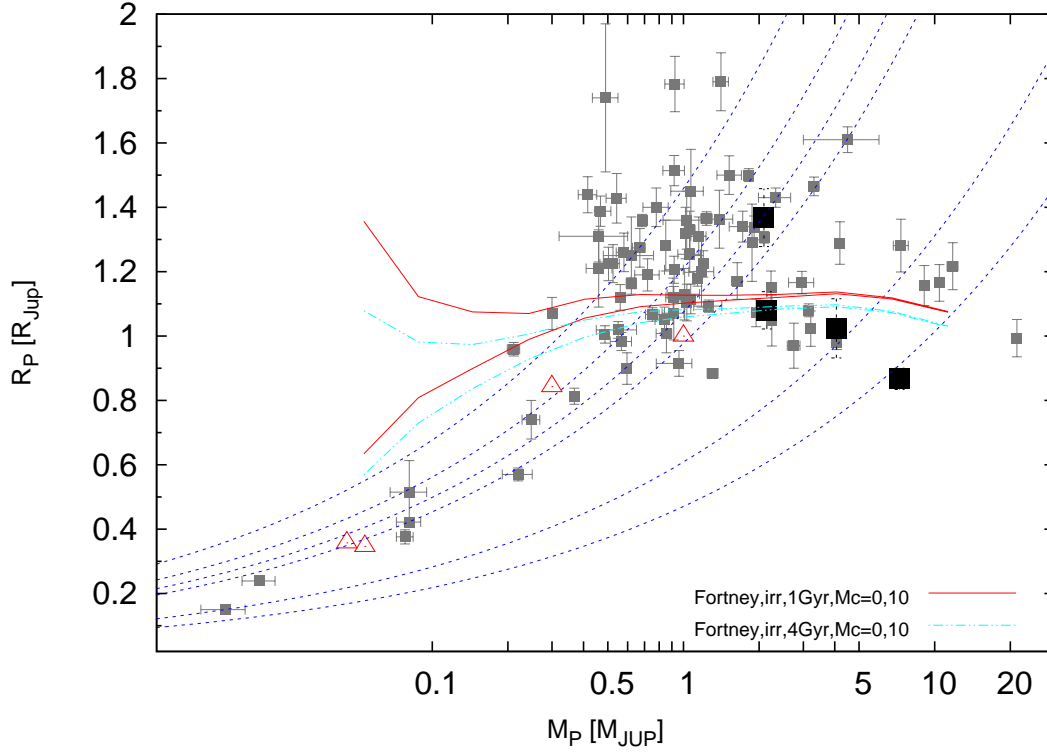


FIG. 16.— Mass-radius diagram of known TEPs (small filled squares). HAT-P-20b–HAT-P-23b are shown as large filled squares. Overlaid are Fortney et al. (2007) planetary isochrones interpolated to the solar equivalent semi-major axis of HAT-P-20b for ages of 1.0 Gyr (upper, solid lines) and 4 Gyr (lower dashed-dotted lines) and core masses of 0 and 10 M_{\oplus} (upper and lower lines respectively), as well as isodensity lines for 0.4, 0.7, 1.0, 1.33, 5.5 and 11.9 g cm^{-3} (dashed lines). Solar system planets are shown with open triangles.

- Bakos, G. Á., Noyes, R. W., Kovács, G., Stanek, K. Z., Sasselov, D. D., & Domsa, I. 2004, *PASP*, 116, 266
- Bakos, G. Á., et al. 2007, *ApJ*, 670, 826
- Bakos, G. Á., et al. 2010, *ApJ*, 710, 1724
- Baglin, A., et al. 2006, 36th COSPAR Scientific Assembly, 36, 3749
- Baraffe, I., Chabrier, G., & Barman, T. 2008, *A&A*, 482, 315
- Baraffe, I., Chabrier, G., & Barman, T. 2010, *Reports on Progress in Physics*, 73, 016901
- Borucki, W. J., et al. 2010, *Science*, 327, 977
- Bramich, D. M. 2008, *MNRAS*, 386, L77
- Buchhave, L. A., et al. 2010, *ApJ*, in press, arXiv:1005.2009
- Butler, R. P. et al. 1996, *PASP*, 108, 500
- Carpenter, J. M. 2001, *AJ*, 121, 2851
- Casagrande, L., Portinari, L., & Flynn, C. 2006, *MNRAS*, 373, 13
- Chatterjee, S., Ford, E. B., Matsumura, S., & Rasio, F. A. 2008, *ApJ*, 686, 580
- Christian, D. J., et al. 2009, *MNRAS*, 392, 1585
- Claret, A. 2004, *A&A*, 428, 1001
- Deleuil, M., Deeg, H. J., Alonso, R., Bouchy, F., & Rouan, D. 2008, *A&A*, 491, 889
- Djupvik, A. A., & Andersen, J. 2010, in “Highlights of Spanish Astrophysics V” eds. J. M. Diego, L. J. Goicoechea, J. I. González-Serrano, & J. Gorgas (Springer: Berlin), p. 211
- Dobbs-Dixon, I., Lin, D. N. C., & Mardling, R. A. 2004, *ApJ*, 610, 464
- Droege, T. F., Richmond, M. W., & Sallman, M. 2006, *PASP*, 118, 1666
- Fabrycky, D., & Tremaine, S. 2007, *ApJ*, 669, 1298
- Ford, E. 2006, *ApJ*, 642, 505
- Ford, E. B., & Rasio, F. A. 2008, *ApJ*, 686, 621
- Fortney, J. J., Lodders, K., Marley, M. S., & Freedman, R. S. 2008, *ApJ*, 678, 1419
- Fortney, J. J., Marley, M. S., & Barnes, J. W. 2007, *ApJ*, 659, 1661
- Fortney, J. J., Baraffe, I., & Militzer, B. 2009, arXiv:0911.3154
- Gandolfi, D. et al. 2010, submitted to *A&A*.
- Gray, D. F. 1992, *Camb. Astrophys. Ser.*, Vol. 20,
- Hansen, B. M. S., & Barman, T. 2007, *ApJ*, 671, 861
- Hartman, J. D., et al. 2009, *ApJ*, 706, 785
- Johnson, J. A., Winn, J. N., Cabrera, N. E., & Carter, J. A. 2008, *ApJ*, 692, L100
- Kipping, D. M., & Bakos, G. Á. 2010, submitted to *ApJ*, arXiv:1004.3538
- Koch, D. G., et al. 2010, *ApJ*, 713, L131
- Kovács, G., Zucker, S., & Mazeh, T. 2002, *A&A*, 391, 369
- Kovács, G., Bakos, G. Á., & Noyes, R. W. 2005, *MNRAS*, 356, 557
- Kovács, G., et al. 2010, *ApJ* submitted, arXiv:1005.5300
- Latham, D. W. 1992, in *IAU Coll. 135, Complementary Approaches to Double and Multiple Star Research*, ASP Conf. Ser. 32, eds. H. A. McAlister & W. I. Hartkopf (San Francisco: ASP), 110
- Leconte, J., Baraffe, I., Chabrier, G., Barman, T., & Levrard, B. 2009, *A&A*, 506, 385
- Levrard, B., Winisdoerffer, C., & Chabrier, G. 2009, *ApJ*, 692, L9
- Queloz, D., et al. 2010, arXiv:1006.5089
- Pál, A., & Bakos, G. Á. 2006, *PASP*, 118, 1474
- Pál, A. 2009, *MNRAS*, 396, 1737
- Pál, A. 2009b, arXiv:0906.3486, PhD thesis
- Perryman, M. A. C., et al., 1997, *A&A*, 323, 49
- Press, W. H., Teukolsky, S. A., Vetterling, W. T. & Flannery, B. P., 1992, *Numerical Recipes in C: the art of scientific computing*, Second Edition, Cambridge University Press
- Mandel, K., & Agol, E. 2002, *ApJ*, 580, L171
- Marcy, G. W., & Butler, R. P. 1992, *PASP*, 104, 270
- McCullough, P. R., Stys, J. E., Valenti, J. A., Fleming, S. W., Janes, K. A., & Heasley, J. N. 2005, *PASP*, 117, 783
- Naef, D., et al. 2001, *A&A*, 375, L27
- Pál, A., et al. 2008, *ApJ*, 680, 1450
- Ramírez, I., & Meléndez, J. 2005, *ApJ*, 626, 465
- Queloz, D., et al. 2009, *A&A*, 506, 303

- Pollacco, D. L., et al. 2006, *PASP*, 118, 1407
- Pourteau, A. 1933, *Catalogue des étoiles doubles de la zone +24 degrés de la Carte Photographique du Ciel*, Observatoire de Paris
- Schlaufman, K. C. 2010, *ApJ*, 719, 602
- Shkolnik, E., et al. 2009, *American Institute of Physics Conference Series*, 1094, 275
- Skiff, B. A. 2009, *VizieR Online Data Catalog*, 1, 2023
- Skrutskie, M. F., et al. 2006, *AJ*, 131, 1163
- Southworth, J., et al. 2009, *ApJ*, 707, 167
- Sozzetti, A. et al. 2007, *ApJ*, 664, 1190
- Tingley, B., & Sackett, P. D. 2005, *ApJ*, 627, 1011
- Torres, G., Neuhauser, R., & Guenther, E. W. 2002, *AJ*, 123, 1701
- Torres, G. et al. 2007, *ApJ*, 666, 121
- Torres, G., et al. 2010, *ApJ*, 715, 458
- Udry, S., Mayor, M., Naef, D., Pepe, F., Queloz, D., Santos, N. C., & Burnet, M. 2002, *A&A*, 390, 267
- Valenti, J. A., & Fischer, D. A. 2005, *ApJS*, 159, 141
- Valenti, J. A., & Piskunov, N. 1996, *A&AS*, 118, 595
- Vogt, S. S. et al. 1994, *Proc. SPIE*, 2198, 362
- Yi, S. K. et al. 2001, *ApJS*, 136, 417
- Vaughan, A. H., Preston, G. W., & Wilson, O. C. 1978, *PASP*, 90, 267
- Winn, J. N., Fabrycky, D., Albrecht, S., & Johnson, J. A. 2010, *ApJ*, 718, L145

